Single-molecule imaging of chromatin remodelers reveals role of ATPase in promoting fast kinetics of target search and dissociation from chromatin

Jee Min Kim[1], Pat Visanpattanasin[1,5], Vivian Jou[1,5], Sheng Liu[1], Xiaona Tang[1], Qinsi Zheng[2], Kai Yu Li[1], Jonathan Snedeker[1], Luke D. Lavis[2], Timothée Lionnet[3], Carl Wu[1,4,*]

[1]Department of Biology, Johns Hopkins University, Baltimore, MD 21218, USA

[2]Janelia Research Campus, Howard Hughes Medical Institute, Ashburn, VA 20147, USA

[3]Institute of Systems Genetics, Langone Medical Center, New York University, New York, NY 10016, USA

[4]Department of Molecular Biology and Genetics, Johns Hopkins School of Medicine, Baltimore, MD 21287, USA

[5]These authors contributed equally

[*]Correspondence: wuc@jhu.edu

ABSTRACT

Conserved ATP-dependent chromatin remodelers establish and maintain genome-wide chromatin architectures of regulatory DNA during cellular lifespan, but the temporal interactions between remodelers and chromatin targets have been obscure. We performed live-cell single-molecule tracking for RSC, SWI/SNF, CHD1, ISW1, ISW2, and INO80 remodeling complexes in budding yeast and detected hyperkinetic behaviors for chromatin-bound molecules that frequently transition to the free state for all complexes. Chromatin-bound remodelers display notably higher diffusion than nucleosomal histones, and strikingly fast dissociation kinetics with 4-7 s mean residence times. These enhanced dynamics require ATP binding or hydrolysis by the catalytic ATPase, uncovering an additional function to its established role in nucleosome remodeling. Kinetic simulations show that multiple remodelers can repeatedly occupy the same promoter region on a timescale of minutes, implicating an unending 'tug-of-war' that controls a temporally shifting window of accessibility for the transcription initiation machinery.

KEYWORDS

ATP-dependent chromatin remodelers, single-molecule tracking, live-cell imaging, search and residence times, promoter region occupancy

INTRODUCTION

Eukaryotic chromatin is assembled in nucleosomes and higher order structures that compact the DNA for genome folding in the cell nucleus. Nucleosomes are actively organized at promoter and enhancer elements that are hypersensitive to nuclease digestion (Almer & Hörz, 1986; Heintzman et al., 2007; Wu, 1980). In the budding yeast *Saccharomyces cerevisiae*, gene promoters contain nucleosome-depleted regions (NDRs), approximately 150 base-pair stretches of DNA that are depleted of nucleosomes (Yuan et al., 2005). Non-canonical nucleosome conformations, often called 'fragile nucleosomes', and non-histone protein-DNA complexes, are also observed by limited MNase treatment and occupy a subset of NDRs (Floer et al., 2010; Kubik et al., 2015; Prajapati, Ocampo, & Clark, 2020). NDRs are flanked by well-positioned +1 and -1 nucleosomes, with the +1 nucleosome overlapping the transcription start site (TSS) in

yeast (Albert et al., 2007; Yuan et al., 2005). The +1 nucleosome also phases downstream nucleosome positions in regularly spaced locations which become progressively less well-positioned into the gene body (Lai & Pugh, 2017a; Mavrich et al., 2008). This arrangement of nucleosomes is important for the accurate engagement of transcription regulators and the transcription pre-initiation complex [PIC], as well as the progression of the transcription machinery after initiation.

ATP-dependent chromatin remodelers are key *trans*-acting factors in establishing and maintaining nucleosome organization around genes (Becker & Workman, 2013; Rando & Winston, 2012; Zhang et al., 2011). As specialized members of the superfamily 2 (SF2) translocases, chromatin remodeling enzymes share a highly conserved ATPase motor that utilizes DNA translocation as the fundamental mechanism to restructure DNA-histone contacts within nucleosomes. In addition to the core ATPase domain, chromatin remodelers harbor additional functional domains and accessory subunits, forming multiprotein complexes up to ~1 MDa in size that show substantial functional diversity. They are further classified into four sub-families based on sequence homology of the catalytic ATPase and possession of shared components, namely the SWI/SNF [Switch defective/sucrose non-fermenting], CHD [Chromodomain helicase DNA-binding], ISWI [Imitation switch], and INO80 [Inositol requiring 80] sub-families.

In vivo studies of remodelers in yeast revealed their distinct genome-wide specificities and functions in the multi-stage transcription process (Yen, Vinayachandran, Batta, Koerber, & Pugh, 2012). In this context, remodelers can be distinguished based on their *in vivo* specificities for nucleosome targets genome-wide. The first group of remodelers, RSC, SWI/SNF, INO80, and ISW2, mainly act at gene promoter regions to define the +1 and -1 nucleosome positions. RSC and SWI/SNF mobilize the +1 and -1 nucleosomes away from the NDR relative to the TSS to promote proper engagement of transcription initiation machinery (Ganguli, Chereji, Iben, Cole, & Clark, 2014; Klein-Brill, Joseph-Strauss, Appleboim, & Friedman, 2019; Kubik et al., 2018). Specifically, RSC assists NDR formation for the majority of yeast genes, and the consequence of conditional RSC inactivation is a global loss of transcription (Brahma & Henikoff, 2019; Ganguli et al., 2014;

Kubik et al., 2018; Yen et al., 2012). This has led to the concept of RSC (and SWI/SNF) as nucleosome 'pushers,' widening the NDR (Kubik et al., 2019). Antagonizing the pushing actions of RSC and SWI/SNF are INO80 and ISW2 (Klein-Brill et al., 2019; Kubik et al., 2019; Shimada et al., 2008; Yen et al., 2012). Both ISW2 and INO80 remodelers reposition the +1 and -1 nucleosomes towards the NDR *in vivo*, which is important for suppressing yeast cryptic transcription via noncanonical TSS usage (Klein-Brill et al., 2019; Kubik et al., 2019; Whitehouse, Rando, Delrow, & Tsukiyama, 2007).

The second group of remodelers, CHD1 and ISW1, act primarily in the gene body where they maintain proper nucleosome spacing and density relative to the +1 nucleosome. Their actions are coupled to transcription elongation by interacting with the elongating polymerase to maintain nucleosome density and thus suppress cryptic initiation within the gene body (Cheung et al., 2008; Radman-Livaja et al., 2012; Smolle et al., 2012a). Remodelers with similar *in vivo* activities are functionally redundant as shown by stronger effects due to multiple deletions or depletions, compared to single deletion or depletion (Kubik et al., 2019; Ocampo, Chereji, Eriksson, & Clark, 2016). Furthermore, remodelers act competitively to fine-tune nucleosome positions around genes, leading to proper transcriptional regulation (Kubik et al., 2019; Ocampo et al., 2016; Ocampo, Chereji, Eriksson, & Clark, 2019; Parnell, Schlichter, Wilson, & Cairns, 2015). These results further highlight the current perspective that nucleosomes located around genes are highly dynamic rather than static, and that the concerted actions of multiple remodelers result in the striking steady-state nucleosome organization observed by genome-wide mapping experiments. However, despite this knowledge, a gap still lies in our understanding of their real-time dynamics and timescales of remodeler interactions on their chromatin targets.

Here we utilize single-molecule tracking (SMT) to directly observe and characterize the chromatin-binding kinetics of ATP-dependent chromatin remodelers in living cells (Lionnet & Wu, 2021). We investigated a comprehensive set of remodelers (RSC, SWI/SNF, CHD1, ISW1, ISW2, INO80) acting at gene promoter regions and gene bodies, allowing us to quantify and compare their *in vivo* dynamics. We show that remodelers

121 have varying but substantial frequencies of chromatin binding, while exhibiting a common
122 target search strategy of frequently engaging in highly transient (sub-second) chromatin
123 interactions and stable residence times of only several seconds. We also discovered that
124 the catalytic ATPase is responsible for enhancing their chromatin-associated diffusion
125 and fast dissociation rates. By integrating the kinetic parameters measured for individual
126 chromatin remodelers with values from genomic studies, we could simulate substantial
127 temporal occupancies at yeast chromatin targets, leading to a tug-of-war model for the
128 organization and dynamic positioning of the nucleosome landscape.
129
130 **RESULTS**
131 **Chromatin remodelers exist in chromatin bound and free populations**
132 We tagged the catalytic subunits of 6 major chromatin remodeling complexes, RSC,
133 SWI/SNF, CHD1, ISW1 (ISW1a, and ISW1b), ISW2, and INO80 at the C-terminus with
134 the self-labeling HaloTag by engineering the endogenous loci and expressed the fusion
135 proteins as the sole source under natural promoter control. The fusion proteins were
136 localized in the nucleus and did not display detectable cleavage of the tag by SDS-PAGE
137 (Figure 1-figure supplement 1A,B). Furthermore, no phenotypes were observed for all
138 strains containing tagged constructs (Figure 1-figure supplement 1C). We then
139 investigated their endogenous, real-time dynamics as representative subunits of
140 chromatin remodeling complexes by single-molecule tracking (Figure 1A).
141
142 In order to quantify a broad range of kinetic behaviors displayed by remodelers, two
143 imaging regimes were applied. 'Fast-tracking' acquires 10 ms frame-rate movies to
144 directly measure a range of single-molecule diffusivities from 'slow' (chromatin-bound) to
145 'fast' (chromatin-free) and determine fractional representation (Figure 1B). However, high
146 laser power and extensive photobleaching precludes measurement of chromatin
147 residence times. 'Slow-tracking' with a longer 250 ms frame-rate and lower laser power
148 motion-blurs fast diffusing molecules to selectively visualize the chromatin-bound state
149 and report dwell times (Figure 1C). Combining the two imaging regimes provides a holistic
150 and quantitative view of a range of diffusive behaviors and kinetic subpopulations.
151

152 We applied two independent methods for visualization and quantification of fast-tracking
153 datasets. First, we determined the diffusion coefficient D for trajectories ≥ 6 frames (i.e.
154 ≥ 60 ms) based on their mean squared displacements (MSD), and present frequency
155 histograms based on the log(D) values of each trajectory. The histograms were fit to two
156 Gaussian distributions, representing slow and fast subpopulations (Figure 1-source data
157 1). For more robust quantification, we applied Spot-On analytics, which uses kinetic
158 modeling based on distribution of displacements for trajectories lasting ≥ 3 frames
159 (Hansen et al., 2018) (Figure 1-figure supplement 2A,B). Hereafter, we refer to diffusive
160 values derived from Spot-On in the text. As previously reported for biological controls,
161 H2B histone (Halo-H2B) and free HaloTag (Halo-NLS, nuclear localization signal), exhibit
162 two distinct, well-separated diffusion states representing chromatin-bound and chromatin-
163 free molecules (Ranjan et al., 2020). We found that the majority of H2B molecules (79.4
164 ± 1.9%) are slow-moving with average D of 0.026 $\mu m^2 s^{-1}$ (Figure 1-figure supplement 2A)
165 consistent with incorporation into chromatin, whereas most of the chromatin-free Halo-
166 NLS molecules show greatly increased diffusivity (D ~ 5 $\mu m^2 s^{-1}$) (Ranjan et al., 2020).
167

168 Compared to H2B, chromatin remodelers exhibit a slow D_{bound} fraction (average 0.036 ±
169 0.007 to 0.067 ± 0.004 $\mu m^2 s^{-1}$) as would be expected for molecules associated with
170 largely immobile chromatin (Figure 1-figure supplement 2A). However, as discussed later,
171 the D_{bound} values are ~2-fold higher than H2B. Furthermore, we also observed a separable
172 chromatin-free fraction whose D_{free} values (0.464 ± 0.043 to 1.014 ± 0.024 $\mu m^2 s^{-1}$) are
173 ~10-fold higher, but distinctly lower than the D_{free} for Halo-NLS, indicating that our imaging
174 regime captures essentially the full range of potential diffusive behaviors for this family.
175 In addition, the D_{free} values show an inverse correlation with the estimated total molecular
176 weights of chromatin remodeling complexes, consistent with expectations that the tagged
177 catalytic subunits are associated within larger complexes (Figure 1-figure supplement 1D).

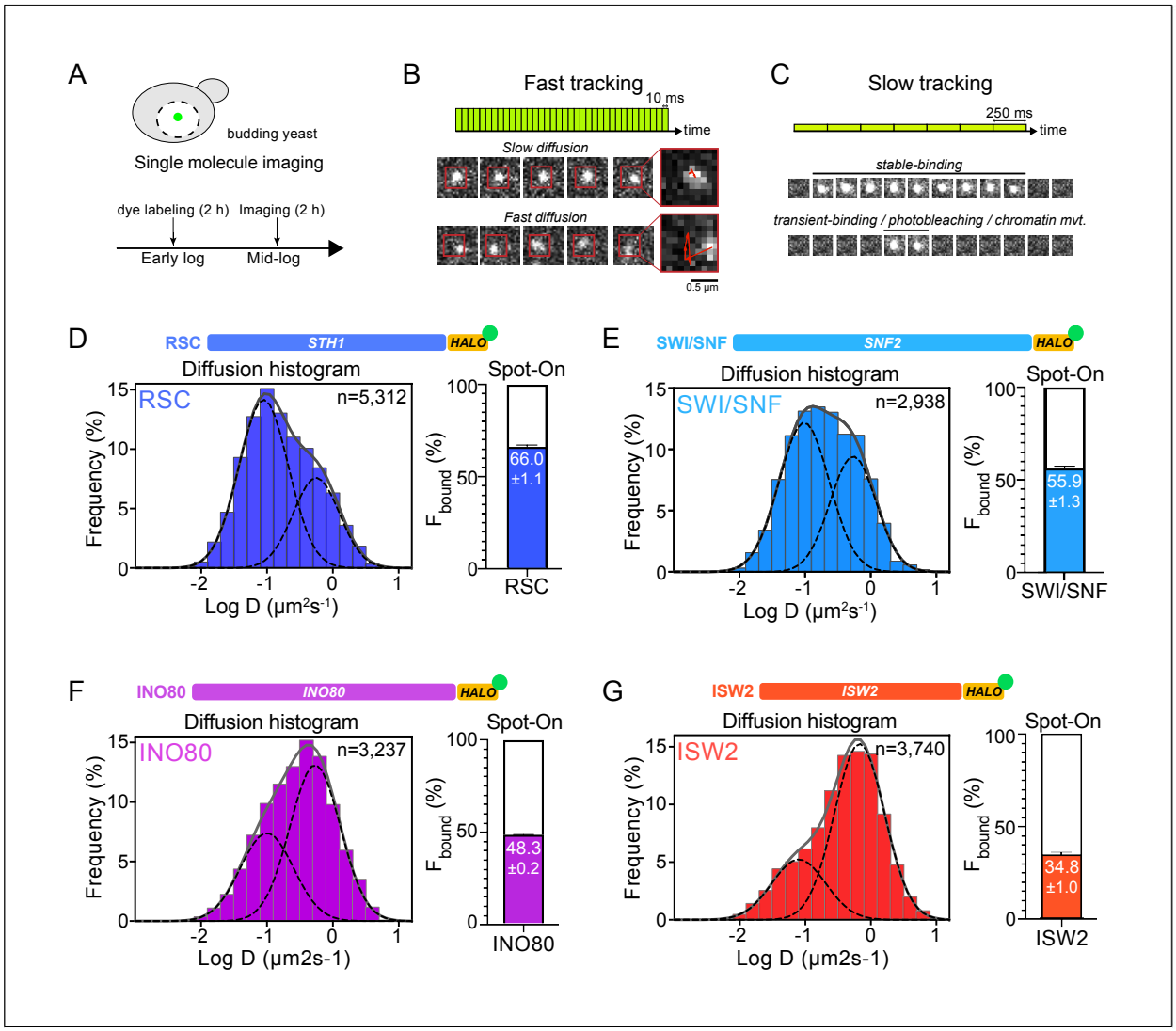

Figure 1. Chromatin-binding and chromatin-free fractions of RSC, SWI/SNF, INO80, and ISW2. Diffusion coefficient histograms show the chromatin-binding fraction is highest for RSC among gene promoter-acting remodelers. **(A)** Experimental scheme. **(B)** Fast-tracking imaging regime uses short exposures (10 ms) at high laser power to distinguish slow (chromatin-bound) and fast (chromatin-free) diffusing populations. **(C)** Slow-tracking regime directly observes the dwell times of chromatin-bound molecules using 250 ms exposures at low laser power. **(D-G)** Fast-tracking diffusion histograms for Sth1-Halo **(D)**, Snf2-Halo **(E)**, Ino80-Halo **(F)**, and Isw2-Halo **(G)**. Left: normalized histograms of $\log_{10}$ diffusion coefficients of single-molecule trajectories fitted to two Gaussian distribution functions (solid gray line: sum of two Gaussians; dashed lines: individual Gaussian curves representing chromatin-bound and chromatin-free populations). Histograms combined from 2 or 3 biological replicates are resampled 100 times by the bootstrap method for resampling errors. Right: Spot-On kinetic modeling results based on displacement distribution histograms. Solid colored bar with indicated value represents % chromatin-bound molecules; open bar represents % chromatin-free. Error bars are standard deviations from 2 or 3 biological replicates.

Figure supplement 1. Cell growth, integrity, and localization of HaloTagged remodeler subunits.
Figure supplement 2. Spot-On kinetic modeling analyses.
Source data 1. MSD-based kinetic analysis results.

178

179 We next assessed how the fractions of chromatin-bound and chromatin-free molecules
180 vary among subgroups of chromatin remodeling enzymes. RSC and SWI/SNF mobilize
181 +1 and -1 nucleosomes to increase promoter accessibility, while INO80 and ISW2
182 mobilize them to reduce accessibility (Hartley & Madhani, 2009; Kubik et al., 2019). We
183 found that the majority of both RSC and SWI/SNF molecules are associated with
184 chromatin (RSC: 66.0 ± 1.1%; SWI/SNF: 55.9 ± 1.3%) (Figure 1D,E). INO80 and ISW2
185 exhibit F_{bound} values of 48.3 ± 0.2% and 34.8 ± 0.4%, respectively (Figure 1F,G). Overall,
186 these NDR-acting remodelers display a broad range of chromatin-binding fractions
187 (inclusive of stable and transient binding), with RSC showing the highest overall
188 chromatin binding.

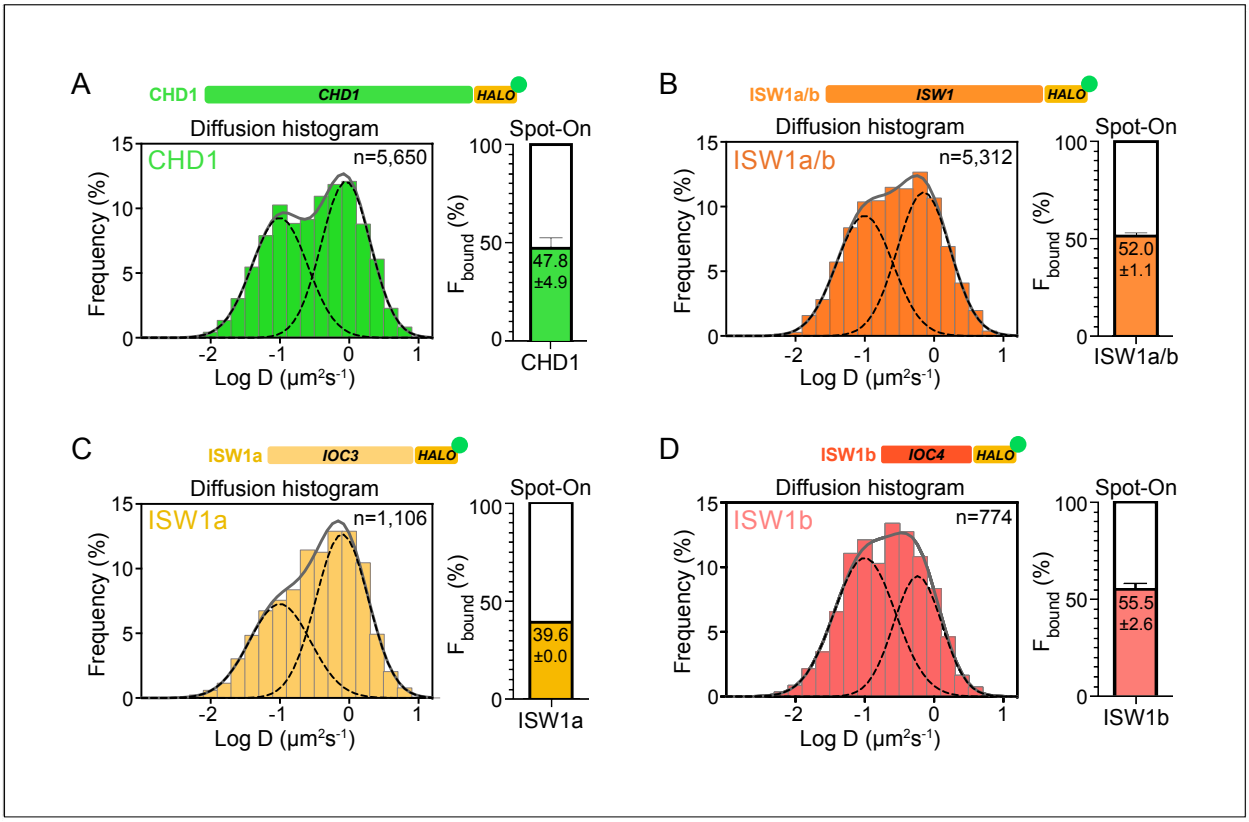

Figure 2. Chromatin-binding and chromatin-free populations of CHD1 and ISW1.
(A-B) Diffusion coefficient histograms and Spot-On analysis as described in Figure 1 for the catalytic subunits Chd1-Halo (A) and Isw1-Halo **(B)**. **(C-D)** Diffusion coefficient histograms and Spot-On analysis of the accessory subunits of ISW1a and ISW1b complexes: Ioc3-Halo **(C)** and Ioc4-Halo **(D)**.

189

190 CHD1 and ISW1 act primarily on nucleosomes located in the gene body (Kubik et al.,
191 2019; Ocampo et al., 2016). The two remodelers show comparable F_{bound} values (CHD1:

192 47.8 ± 4.9%; ISW1a/b: 52.0 ± 1.1%) (Figure 2A,B). However, the catalytic subunit Isw1
193 is shared by two distinct chromatin remodeling complexes called ISW1a and ISW1b (Vary
194 et al., 2003), in addition to potentially un-complexed Isw1 catalytic subunit (Tsukiyama,
195 Palmer, Landel, Shiloach, & Wu, 1999). The ISW1a complex localizes near the
196 transcription start and end of genes, whereas the ISW1b complex occupies more mid-
197 coding regions (Morillon et al., 2003; Smolle et al., 2012b; Yen et al., 2012). Since Isw1
198 catalytic subunit dynamics represent a composite of the two remodeling complexes, we
199 also tagged Ioc3 and Ioc4 accessory subunits unique to ISW1a and ISW1b complexes,
200 respectively. The gene-body acting ISW1b (Ioc4-Halo) complex exhibits higher F_{bound}
201 compared to ISW1a (Ioc3-Halo) complex (ISW1b: 55.5 ± 2.6%; ISW1a: 39.6 ± 0.0%)
202 (Figure 2C,D).
203
204 **Chromatin remodelers frequently transition between bound and free states**
205 Unlike the two well-separated Gaussian distributions for H2B histones and HaloTag
206 protein (Figure 3A), the Log(D) histograms of all imaged chromatin remodelers display
207 less distinct bound and free populations, with a noticeable fraction showing an
208 intermediate range of diffusion coefficients (Figure 1D-G, Figure 2). This population could
209 either represent remodeler complexes transitioning between chromatin-bound and
210 chromatin-free states, or chromatin-free molecules of intermediate diffusivity due to
211 association with additional factors or confined inside a subnuclear compartment (Hansen,
212 Amitai, Cattoglio, Tjian, & Darzacq, 2020; Izeddin et al., 2014; McSwiggen et al., 2018;
213 Strom et al., 2017).
214
215 To distinguish between these possibilities, we analyzed single-particle trajectories using
216 vbSPT, a variational Bayesian Hidden Markov Model (HMM) algorithm, which models
217 state kinetics and assigns diffusive states to each displacement (Persson, Lindén,
218 Unoson, & Elf, 2013). We classified every displacement as either State 1 ('bound') or
219 State 2 ('free') (Figure 3-source data 1), and sub-classified all trajectories as bound, free,
220 or transitioning (Figure 3B). The median bound and free displacement lengths between
221 transitioning and non-transitioning trajectories are highly similar or identical for each
222 remodeler, validating the vbSPT state assignments and essentially excluding a dominant

223 intermediate diffusive state (Figure 3-figure supplement 1A-C). Notably, the log D
224 histograms of transitioning populations show enrichment for intermediate D values.
225
226

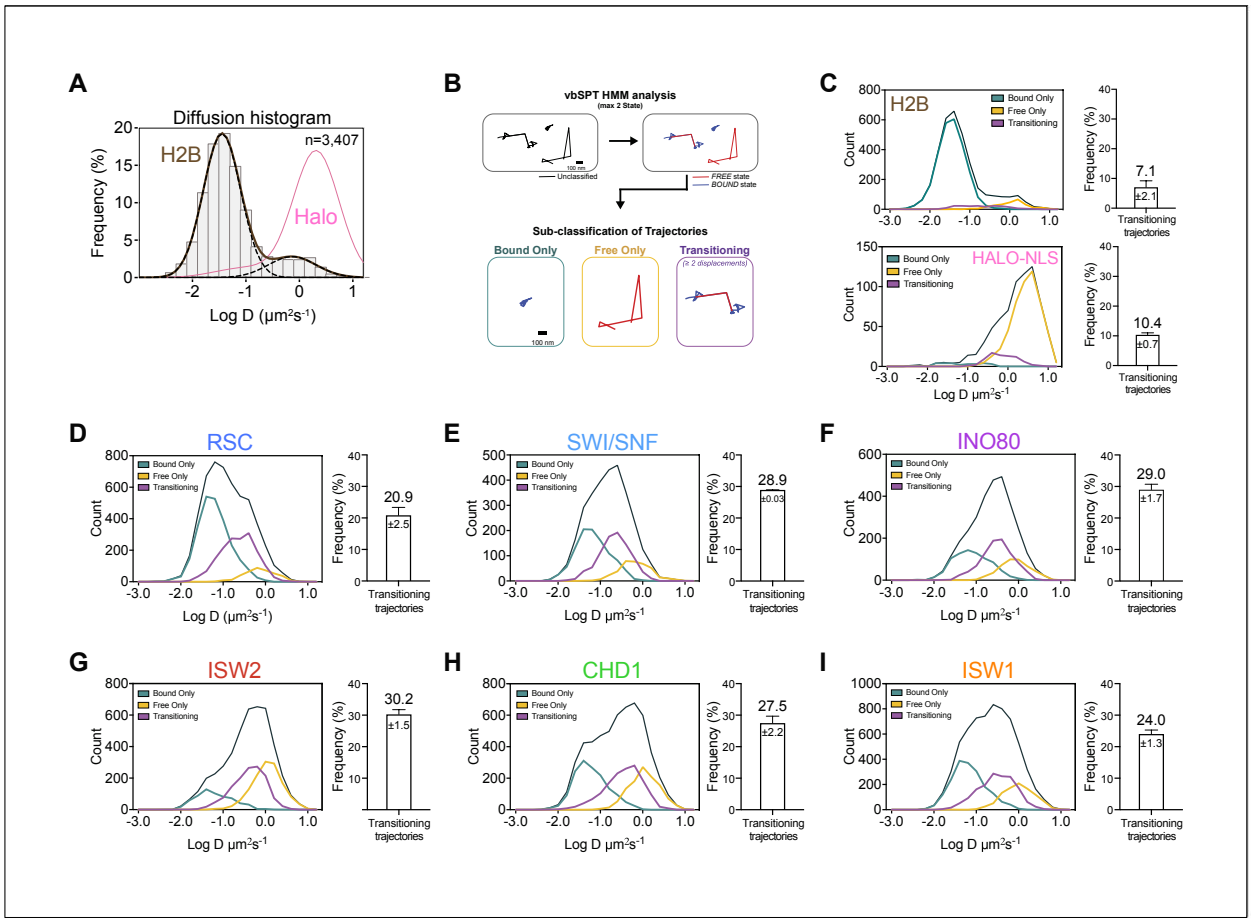

Figure 3. Remodelers undergo frequent transitions between bound and free states.
(A) Halo-H2B (brown) and Halo-NLS (pink) molecules display well-separated peaks in their diffusion coefficient histograms. **(B)** An overview of displacement-based HMM classification (vbSPT) to identify transitioning trajectories. After classifying each displacement as either in bound or free state, each trajectory is sub-classified as 'bound only', 'free only', or 'transitioning'. **(C-I)** Left: Overlay of raw histograms of $\log_{10}$ diffusion coefficients for 'Bound only' (turquoise), 'Free only' (yellow), 'Transitioning' (purple), and total trajectories (thin black). Right: Quantification (%) of transitioning trajectories in the diffusion coefficient histogram, where errors represent standard deviation between 2 or 3 biological replicates.. **(C)** Transitioning trajectories for Halo-H2B (top) and Halo-NLS (bottom). **(D-I)** Transitioning trajectories for remodelers: Sth1-Halo **(D)**, Snf2-Halo **(E)**, Ino80-Halo **(F)**, and Isw2-Halo **(G)**, Chd1-Halo **(H)**, and Isw1-Halo **(I)**.

Figure supplement 1. Validation of two diffusive states classified by vbSPT, and quantification of transitioning frequencies.
Source data 1. vbSPT analysis results.

227

228 It is striking that the population of transitioning trajectories is more prominent for
229 remodelers (from 20.9 ± 2.5% to 30.2 ± 1.5%) compared to free HaloTag (10.4 ± 0.7%)
230 and H2B histone (7.1 ± 2.1%), (Figure 3C-I, Figure 3-figure supplement 1D-E). We
231 observed comparable frequencies for remodeler dissociation (bound to free transition:
232 45.3 ± 1.3 to 50.24 ± 0.01 %) and association (free to bound: 49.76 ± 0.01 to 54.7 ± 1.3%),
233 indicating that there is little bias in the direction of state transitions (Figure 3-figure
234 supplement 1F). Furthermore, the frequent detection of state transitions over short
235 trajectory lifetimes suggests that the duration of each state is short-lived. We concluded
236 that transient but frequent chromatin interactions are characteristic of the six remodeling
237 complexes.
238
239 **All remodelers have remarkably short *in vivo* residence times of 4-7 s**
240 The chromatin-bound remodeler population measured by fast tracking consists of both
241 transiently and stably bound molecules. We acquired long-exposure movies [250
242 ms/frame] under slow tracking (Chen et al., 2014) to generate survival curves revealing
243 the apparent dissociation of chromatin-bound molecules as a function of time (Figure 1C).
244 Particle dissociation can be due to molecules truly disengaging from chromatin, or to
245 fluorophore photobleaching and chromatin movements out of focus, which can corrected
246 using the survival curve of H2B histone as a standard (Hansen, Pustova, Cattoglio, Tjian,
247 & Darzacq, 2017). The remodeler survival plots fit well to a double exponential decay
248 model (Figure 4-figure supplement 1A-F,H), from which the average lifetimes (τ_{sb}, τ_{tb}) and
249 fractions (f_{sb}, f_{tb}) of stable-binding and transient-binding species were extracted (Figure
250 4). All τ values presented in the text and figures are corrected based on H2B decay
251 kinetics.
252
253 The stable-binding subpopulations (f_{sb}) of RSC (27 ± 2%) and SWI/SNF (24 ± 6%) display
254 strikingly short lifetimes (RSC: 5.0 ± 0.7 s; SWI/SNF 4.4 ± 1.2 s) (Figure 4A,B), consistent
255 with a previous measurement for the Rsc2 subunit of RSC (Mehta et al., 2018). Similarly,
256 INO80 and ISW2 exhibit stable-binding fractions (f_{sb} 20 ± 3% and 13 ± 3%, respectively)
257 and similarly short residence times (τ_{sb} 3.7 ± 0.8 s and 4.9 ± 2.2 s, respectively) (Figure
258 4C,D). Hence, all NDR-acting remodelers bind stably for less than 5 s in live yeast,

259 whereas transient-binding populations are more short-lived by almost an order of
260 magnitude (Figure 4-source data 1).
261

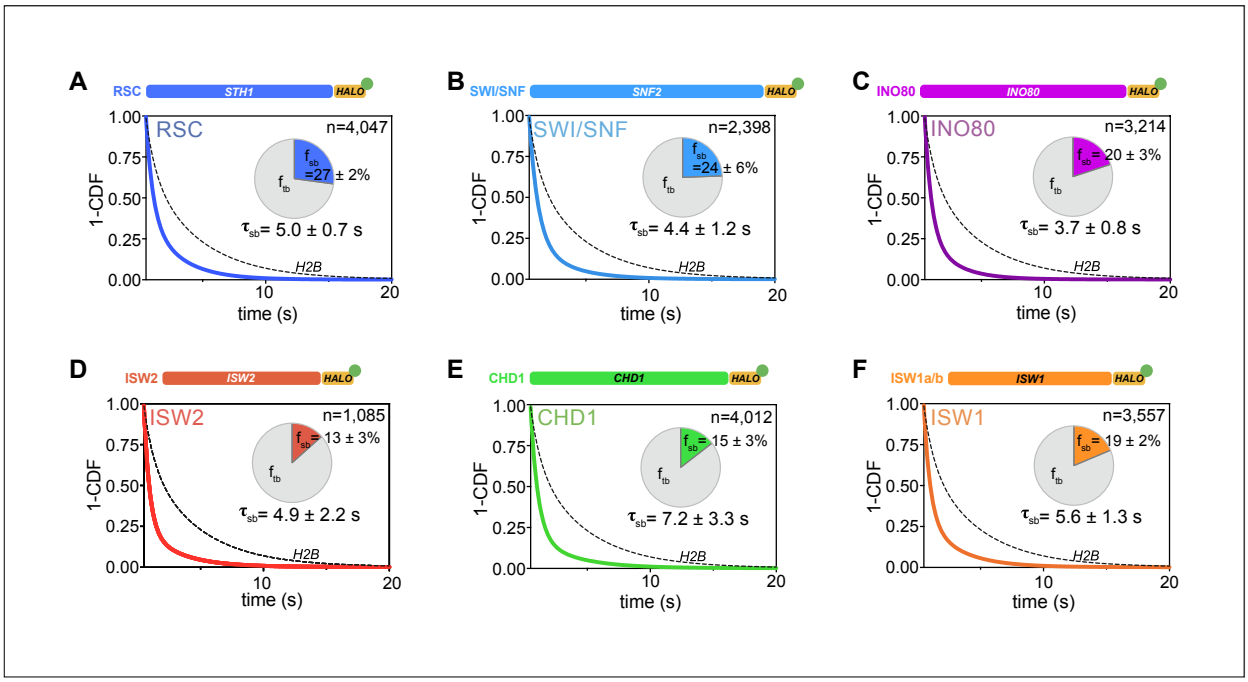

Figure 4. All remodelers have short-lived stable-binding residence times of 4-7 s.
(A-F) Fitted double exponential decay curves from 1-CDF plots of observed dwell times from individual binding events (n) imaged by slow-tracking, for Sth1-Halo **(A)** Snf2-Halo **(B)**, Ino80-Halo **(C)**, and Isw2-Halo **(D)**, Chd1-Halo **(E)**, and Isw1-Halo **(F)**. Solid colored and dashed black fitted curves for indicated remodelers and H2B, respectively. Pie charts show the percentage (f_{sb}) and average residence time (τ_{sb}) of the stable binding population after photobleaching correction. Errors represent bootstrap resampling errors after resampling 100 times (sb: stable-binding; tb: transient-binding).

Figure supplement 1. Survival plots [1-CDF] of dwell times showing 1- vs 2-component exponential decay fits.
Source data 1. Kinetic parameters determined by Slow-tracking.

262

263 For gene body-acting remodelers, CHD1 and ISW1 complexes exhibit stable-binding
264 fractions (f_{sb} 15 ± 3% and 19 ± 2%, respectively) and short dwell times (τ_{sb} 7.2 ± 3.3 s and
265 5.6 ± 1.3 s, respectively) (Figure 4E,F). Interestingly, ISW1b shows 2.5-fold higher
266 residence times compared to ISW1a (τ_{sb} 5.9 ± 2.5 s and 2.2 ± 1.0 s, respectively) with
267 comparable stable-binding fractions (Figure 4-figure supplement 1G). These remodelers
268 also exhibit very short transient-binding residence times (τ_{tb}< 0.65 s). Hence, the majority
269 of chromatin binding events by remodelers is transient, and stable binding, on the order
270 of several seconds, is notably short-lived.

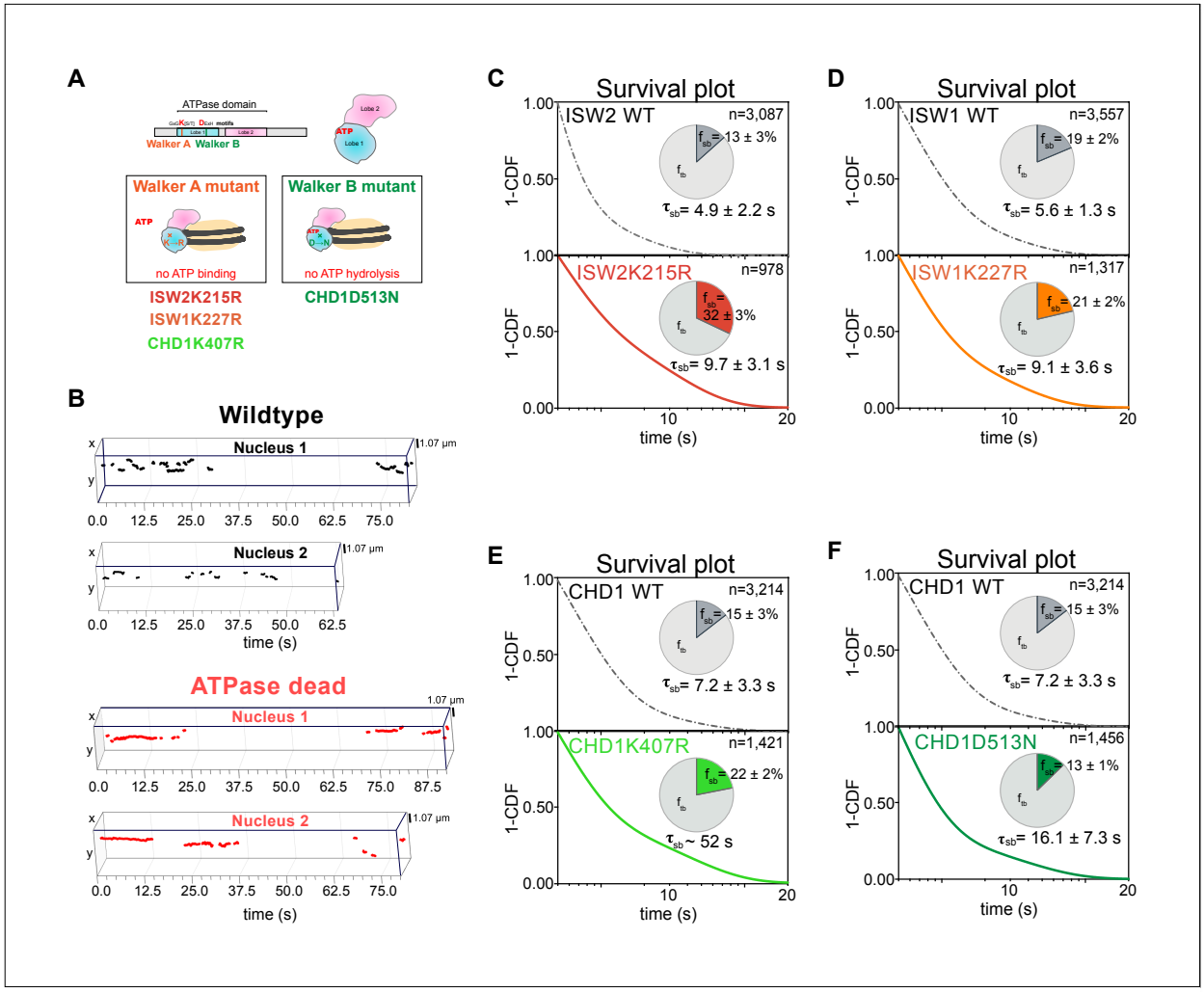

Figure 5. ATP hydrolysis is responsible for rapid chromatin dissociation.
(A) Bar diagram and cartoons for remodelers mutated in the 'Walker A' and 'Walker B' motifs, respectively. **(B)** Representative 3D plots of trajectories imaged by slow-tracking for wildtype (Chd1-Halo, black) and ATPase-dead mutant (Chd1K407R-Halo, red). Each plot shows all trajectories (≥ 3 frames) from single nucleus where lines represent apparent durations of chromatin-binding events. **(C-F)** 1-CDF plot, pie chart, and residence times of wildtype (top) and ATPase-dead mutants (bottom) for Isw2 **(C)**, Isw1 **(D)**, and Chd1 **(E,F)**.

Figure supplement 1. Expression levels and 1-CDF plots for wildtype and mutant ATPase-dead Isw2D312N.
Source data 1. Slow-tracking results for ATPase-dead mutants.

ATPase activity is coupled to fast dissociation rates

To examine whether the measured dissociation kinetics are intrinsic to chromatin remodeling complexes or functionally related to their ATP-dependent remodeling activities, we made strains harboring a point mutation in the ATPase domains of Isw2,

277 Isw1, and Chd1; these mutations have previously been shown to abolish their ATPase
278 activities (Isw2K215R, Isw1K227R, Chd1K407R, and Chd1D513N) (Figure 5A)
279 (Fitzgerald et al., 2004; Gelbart, Rechsteiner, Timothy, Tsukiyama, & Richmond, 2001;
280 Hauk, McKnight, Nodelman, & Bowman, 2010; Tsukiyama et al., 1999). We then acquired
281 slow-tracking movies to compare the dwell times of mutant to those of wildtype
282 remodeling enzymes (Figure 5B)
283
284 We found that the stable-binding average residence time increased by ~2-fold (from 4.9
285 ± 2.2 to 9.7 ± 3.1 s) for the Isw2K215R mutant (Figure 5C). Similarly, we observed
286 increased residence time (from 5.6 ± 1.3 to 9.1 ± 3.6 s) for the Isw1K227R (Figure 5D).
287 The two ATPase-dead Chd1 mutants both showed increased stable-binding residence
288 times (Chd1K407R from 7.2 ± 3.3 to ~52 s; Chd1D513N from 7.2 ± 3.3 to 16.1 ± 7.3 s)
289 (Figure 5E,F). Interestingly, the tail of the Chd1K407R survival curve approaches that of
290 H2B, which indicates its longevity, but precludes precise determination of dwell time
291 (Figure 5-figure supplement 1B). All four mutants (Figure 5-source data 1) exhibit little to
292 no changes in the transient-binding residence times compared to wildtype. In all, our
293 results indicate that after chromatin association, the mutant ATPases exhibit slower
294 dissociation rate (the reciprocal of residence time), consistent with previous genome-wide
295 ChIP and biochemical studies (Fitzgerald et al., 2004; Gelbart et al., 2001).
296
297 **ATP binding enhances chromatin-bound mobility of remodelers**
298 Chromatin imaged by several distinct methods in living cells displays heterogeneous
299 mobility, which is dependent on its compaction state, subnuclear localization, and ATP-
300 dependent processes (Gasser, 2002; Gu et al., 2018; Marshall et al., 1997; Soutoglou &
301 Misteli, 2007). Remodelers may undergo 1D translocation on DNA (Sirinakis et al., 2011),
302 and alter either local chromatin movement (Basu et al., 2020; Neumann et al., 2012) or
303 higher-order chromatin structure (Lusser, Urwin, & Kadonaga, 2005; Maier, Chioda,
304 Rhodes, & Becker, 2008) in an ATP-dependent fashion. We assessed the diffusive
305 behavior of the chromatin-bound fraction of remodelers relative to the average dynamics
306 of incorporated Halo-H2B histone. From each trajectory classified as bound by vbSPT,
307 the apparent D value and the R_c [radius of confinement] were calculated to characterize

308 its diffusivity and the confined domain encompassing the observed trajectory, respectively
309 (Lerner et al., 2020). Importantly, chromatin-bound remodelers exhibit ~2-fold higher
310 mobility than H2B histone, as revealed by the average MSD plot and the distribution of
311 individual D values of each trajectory under fast-tracking (Figure 6A,B). The mean R_c
312 values are also substantially higher for remodelers compared to the global mean
313 measured for H2B (Figure 6-figure supplement 1A). This is further supported by the
314 higher apparent D values to varying degrees [2- to 4-fold] of stably-bound remodelers
315 measured by slow-tracking (Figure 6C). Such greater mobility of chromatin-bound
316 remodelers may be due to the combined effects of remodeler diffusion on chromatin and
317 movement of the chromatin fiber caused by remodeling activity, or alternatively, may
318 reflect the intrinsic dynamics of genomic loci being targeted.
319
320 To distinguish between these two alternatives, we measured the chromatin-associated
321 mobility of the four aforementioned ATPase-dead mutants. Three mutants Isw2K215R,
322 Isw1K227R, Chd1K407R harboring substitutions in the catalytic ATPase Walker A motif
323 responsible for ATP binding display strikingly lower diffusivity as revealed by the average
324 MSD plot of stably bound molecules, which approaches or substantially overlaps the
325 global H2B curve (Figure 6D-F). This is supported by the violin plots of individual D values
326 for stably bound trajectories (Figure 6G). Surprisingly, Chd1D513N bearing a substitution
327 in the Walker B motif of Chd1 shows no substantial changes in the average MSD curve
328 and apparent D values for stably bound trajectories compared to wildtype as measured
329 by slow-tracking (Figure 6F,H). To rule out Chd1-specific effects, we also made a strain
330 harboring the corresponding D-to-N substitution in ISW2 (Isw2D312N), and found no
331 substantial changes in the average MSD curve and apparent D values compared to
332 wildtype (Figure 6D,H). As expected for a mutation in the catalytic ATPase, the
333 Isw2D312N mutant exhibits an approximately two-fold increase in its residence time
334 compared to wildtype (Figure 5-figure supplement 1C). Because the Walker B motif is
335 important for ATP hydrolysis (via coordinating Mg^{2+} ion and a water molecule), but not for
336 ATP binding (Singleton, Dillingham, & Wigley, 2007; Walker, Saraste, Runswick, & Gay,
337 1982) (Figure 5A), this result suggests that the ATP-bound state may be adequate to

induce enhanced diffusion on chromatin as part of the mechanism of target search by remodeling enzymes.

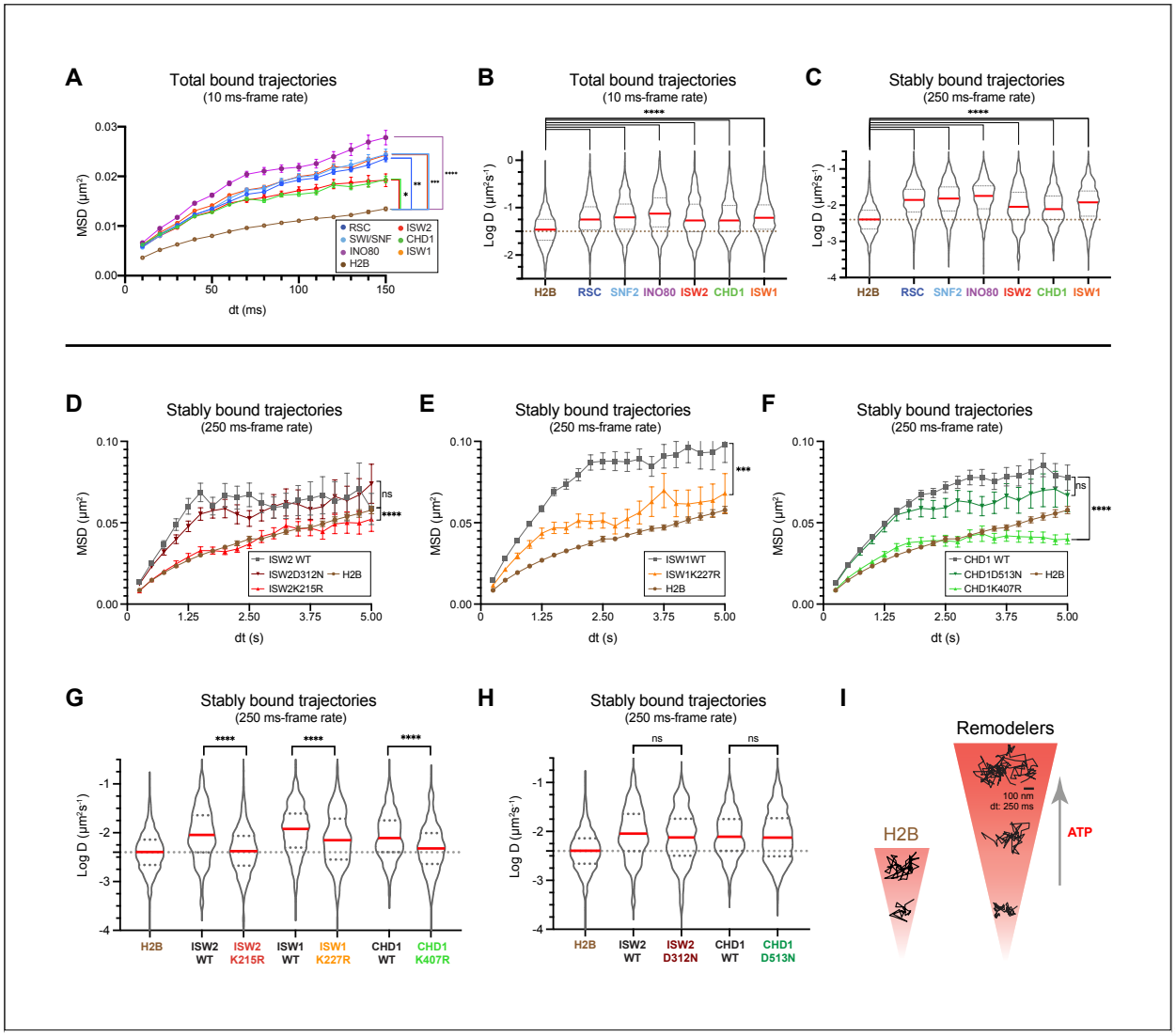

Figure 6. ATP utilization is responsible for enhanced mobility of chromatin-bound remodeler.
(A-B) Average MSD plot **(A)** and violin plot **(B)**, of individual D values for 'bound only' trajectories imaged by fast-tracking, shown for six remodelers and H2B histone. **(C)** Violin plot showing distribution of individual D values imaged by slow-tracking for six remodelers and H2B histone. For **A-C**, each wildtype remodeler is compared to H2B by the ordinary one-way ANOVA test (****p<0.0001, ***p<0.001, **p<0.01, *p<0.05). **(D-H)** MSD plot **(D-F)** and violin plot **(G,H)** of individual D values for trajectories imaged by slow-tracking for wildtype, ATPase-dead mutant, and H2B. For violin plots, thick red and dotted gray lines represent the median and two quartiles, respectively. For **D-H**, mutants are compared to wildtype by the unpaired t test (****p<0.0001, ***p<0.001, ns: not significant). **(I)** Representative trajectories imaged by slow-tracking for H2B and remodelers. H2B displays low mobility, whereas remodelers display higher chromatin-associated diffusivity that is enhanced by ATP utilization.

Figure supplement 1. Chromatin-bound remodelers display higher radius of confinement (Rc) values than H2B.
Source data 1. Number of molecules (N), statistical tests, and source data for Figure 6.

340

341 **Promoter-enriched remodelers have robust chromatin occupancies**

342 Chromatin remodelers are key regulators of the +1 nucleosome position genome-wide,
343 whose accurate location is crucial for the PIC (pre-initiation complex) formation and TSS
344 fidelity (Lai & Pugh, 2017b; Zhang et al., 2011). RSC and SWI/SNF mobilize the +1
345 nucleosome away from the NDR, opposed by INO80 and ISW2 activities, which slide the
346 +1 nucleosome towards the NDR. As a quantitative indicator of nucleosome engagement,
347 we determined the occupancies of the four remodelers, i.e. the percent average
348 occupancy at a chromatin target by each remodeler over a given time period. To calculate
349 temporal occupancy, we utilized the measured overall chromatin-binding fraction [F_{sb}] and
350 the temporal parameters for stable [τ_{sb}, f_{sb}] and transient [τ_{tb}, f_{tb}] chromatin-binding (Figure
351 7A). Here, we assume that stable binding, which is almost an order of magnitude longer
352 than transient binding, represents binding at 'specific' target sites within promoter regions
353 including -1, +1 nucleosomes and the intervening NDR, while transient binding represents
354 non-specific chromatin interactions (Ball et al., 2016).

355

356 The fraction of stable-binding depends on both the number of molecules per nucleus
357 ($N_{molecules}$) and number of the target sites in the genome ($N_{targets}$) (Chen et al., 2014). For
358 $N_{molecules}$, we used published values compiled from orthogonal approaches to determine
359 protein abundance in *S. cerevisiae* (Ho, Baryshnikova, & Brown, 2018). As regards the
360 number of chromatin targets ($N_{targets}$), many studies have investigated the genome-wide
361 specificities of chromatin remodelers using multiple approaches including ChIP-Seq
362 (Cutler, Lee, & Tsukiyama, 2018; Floer et al., 2010; Shimada et al., 2008; Spain et al.,
363 2014), MNase-ChIP (Yen et al., 2012), ChIP-exo (Rossi et al., 2021), Native-ChIP-Seq
364 (Ramachandran, Zentner, & Henikoff, 2015; Zentner, Tsukiyama, & Henikoff, 2013),
365 CUT&RUN (Brahma & Henikoff, 2019), and ChEC-seq (Kubik et al., 2019). For this paper,
366 we utilized the $N_{targets}$ values reported by Kubik *et al.*, who investigated the binding sites
367 for four yeast remodelers of interest in this study, and explicitly quantified the number of
368 mRNA gene promoters enriched for each remodeler. Assuming that the +1 or -1
369 nucleosomes and the NDR together represent the main interaction substrates at promoter
370 regions, this value of $N_{targets}$ can be considered as a lower bound estimate. Accordingly,

371 RSC binding is the most widespread ($N_{targets}$= 3702), SWI/SNF binds only a small subset
372 ($N_{targets}$= 466), and INO80 ($N_{targets}$= 1646) and ISW2 ($N_{targets}$= 1802) each bind to
373 approximately a third of all yeast promoters (Kubik et al., 2019).
374

a

Remodeler	F_{bound}	f_{sb}	Corrected τ_{sb} (s)	Corrected τ_{tb} (s)	$N_{molecules}$*	$N_{targets}$**	N_{trials}	Search time (s)	Sampling interval (s)	**Occupancy (%)**
RSC (Sth1)	0.66	0.27	5.0	0.54	4603 ± 639	3702	15 ± 2.4	15 ± 2.6	16 ± 3.1	**32 ± 7.5**
SWI/SNF (Snf2)	0.56	0.24	4.4	0.68	2307 ± 430	466	13 ± 4.5	19 ± 6.7	4.7 ± 1.6	**93 ± 41**
INO80 (Ino80)	0.48	0.20	3.7	0.55	3782 ± 661	1646	16 ± 4.3	23 ± 6.0	12 ± 3.3	**32 ± 12**
ISW2 (Isw2)	0.35	0.13	4.9	0.44	2554 ± 316	1802	42 ± 20	61 ± 30	47 ± 22	**11 ± 6.8**

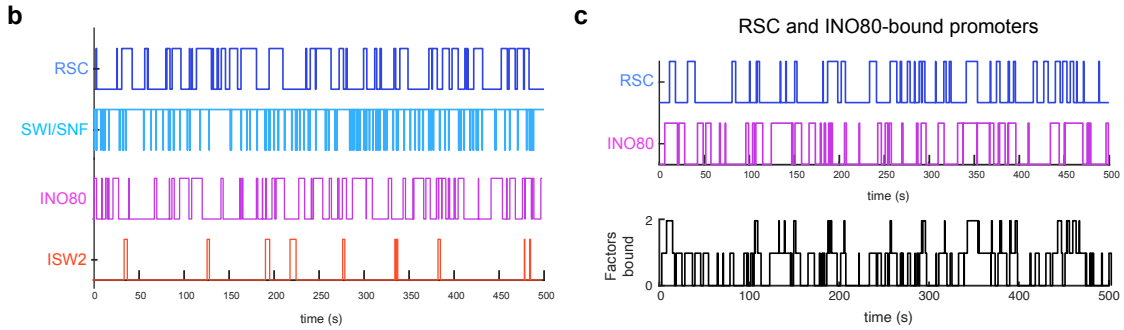

Figure 7. Remodelers show substantial temporal occupancies at chromatin targets.
(A) Key parameters measured in this study and acquired from the literature (Ho et al., 2018; Kubik et al., 2019) are used to calculate occupancy levels for gene promoter-acting remodelers. **(B)** Time trace simulations of temporal occupancy for individual remodelers at a target promoter region based on average τ_{sb} and sampling interval. Top and bottom bars represent occupied (on) and vacant (off) states, respectively, and vertical lines depict transitions between the two states. **(C)** Time trace simulations of occupancy at a RSC- and INO80-bound promoter region based on average τ_{sb} and sampling interval. Individual time trace simulations are shown above, and the cumulative simulated occupancy plot (black) shows either one or both remodelers bound in the time course of 500 s.

Figure supplement 1. Time trace simulations of temporal occupancies at promoters bound by multiple remodelers, and analysis of CHD1 DNA-binding mutant.

375

376 To calculate occupancy values, we used the τ_{search} (search time), the time it takes for a
377 molecule to go from one stable target site to the next [i.e. time bound non-specifically plus
378 time in free diffusion], the SI (sampling interval) [i.e. the time between initial binding of
379 one molecule and binding of the second molecule], and the estimated values for $N_{molecules}$
380 and $N_{targets}$ per cell (Figure 7A; see Methods). RSC shows substantial occupancy (32 ±
381 7.5%) at stably bound chromatin targets, despite its short residence time (τ_{sb}) of 5.0 ± 0.7

382 s. Thus, rather than individual RSC molecules residing for long periods of time, the high
383 occupancy rate can be attributed to the short τ_{search} (15 ± 2.6 s) and comparable SI (16 ±
384 3.1 s) values coupled to high $N_{molecules}$ (>4000) (Figure 7A). SWI/SNF exhibits the highest
385 occupancy (93 ± 41%) among the four remodelers, consistent with the highest raw ChEC
386 signals reported for Swi3 (Kubik et al., 2019). Strikingly, our estimate indicates that
387 SWI/SNF also maintains its occupancy at target sites by coupling short residence time
388 (4.4 ± 1.2 s) with short SI (4.7 ± 1.0 s) (Figure 7A).
389
390 We next assessed the occupancy values for INO80 and ISW2, which oppose the actions
391 of RSC and SWI/SNF. Comparable to RSC, INO80 displays substantial occupancy (32 ±
392 9.2%) at its targets while ISW2 displays a lower occupancy (11 ± 5.0%). INO80 exhibits
393 short τ_{search} (23 ± 6.0 s) and SI (16 ± 4.3 s) values, while ISW2 has a relatively longer
394 τ_{search} (61 ± 30 s) and SI (47 ± 22 s) values (Figure 7A). Average time trace simulations
395 of stably bound occupancies for each of the four remodelers over several hundred
396 seconds (Figure 7B) show that at promoter regions targeted by multiple remodelers such
397 as genes in 'cluster IV' enriched for RSC and INO80 (Kubik et al., 2019), the occupancy
398 by any one remodeler is strikingly high, and more than one remodeler can simultaneously
399 engage a promoter repeatedly over several minutes (Figure 7C; see also Figure 7-figure
400 supplement 1A,B).

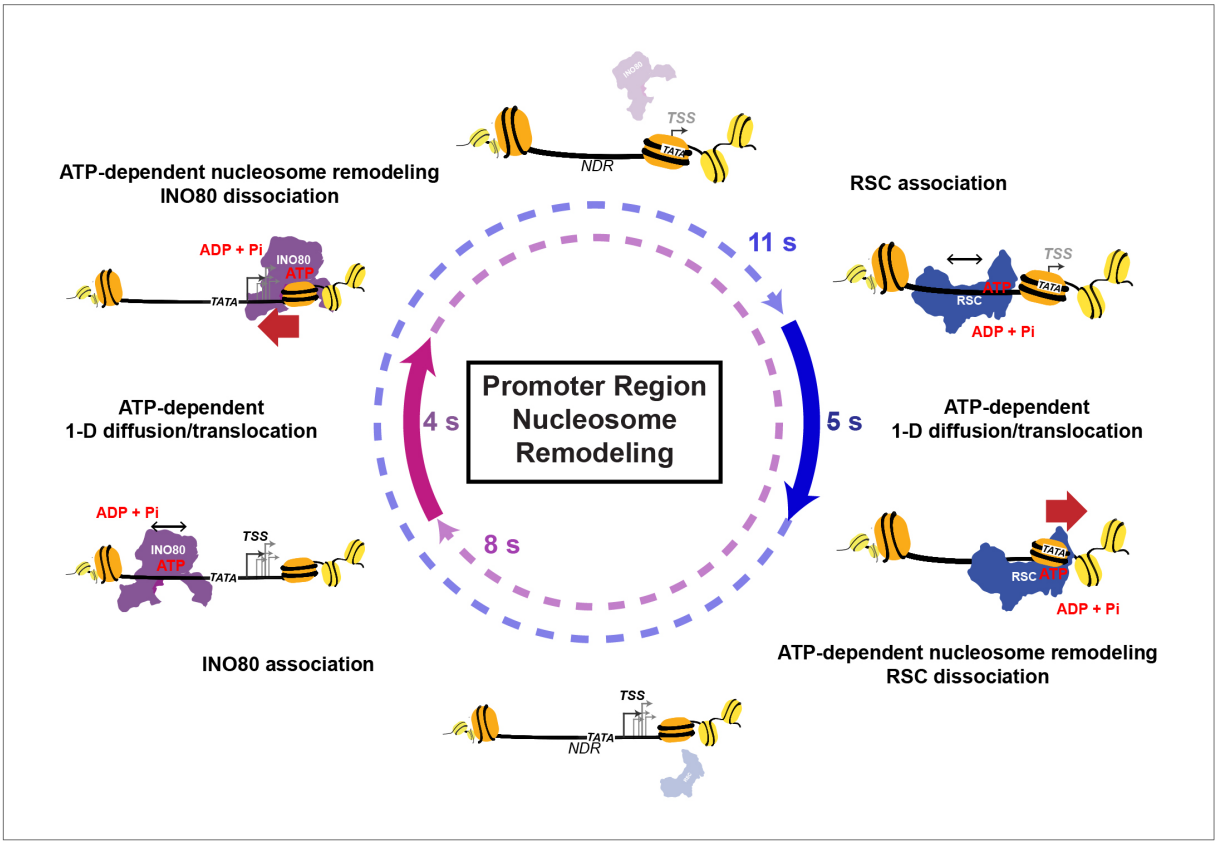

Figure 8. Nucleosome remodeling cycle at NDRs.
Model for nucleosome remodeling cycle at a gene promoter region targeted by RSC and INO80. The promoter region transitions between remodeler-occupied [solid arrow] and -vacant [dashed arrow] states, and their durations are indicated. After association of RSC or INO80 to the NDR, remodelers undergo 1-D diffusion on chromatin in an ATP-dependent manner, resulting in higher chromatin-associated mobility. Upon engaging its nucleosome substrate [e.g. the +1 nucleosome], RSC and INO80 uses the energy of ATP hydrolysis to push or pull the nucleosome away from NDR, respectively. ATP hydrolysis facilitates remodeler dissociation, and the promoter region becomes vacant for other factor interactions. The order of remodeler visitation is arbitrary, and simultaneous co-occupancy within the NDR can occur infrequently (see text for details).

401

402 **DISCUSSION**

403 Imaging chromatin remodeler diffusion by the fast-tracking mode in yeast shows that they
404 bind to chromatin at substantial frequencies [F_{bound}: 35 - 66%], and with a notable
405 population [21 - 30%] displaying intermediate D values resulting from transitions between
406 bound and free states (Figure 1-3). This suggests remodelers frequently undergo highly
407 short-lived chromatin interactions and is consistent with our slow-tracking measurements
408 of transient-binding frequency (f_{tb}: 73 - 87%) (Figure 4), and with FRAP and FCS
409 measurements of over-expressed mammalian ISWI (Erdel, Schubert, Marth, Längst, &

410 Rippe, 2010). The high frequency of transient interactions, and direct evidence for
411 transitioning trajectories is also consistent with the model of 1D-3D facilitated diffusion, a
412 proposed mechanism to increase the target search efficiency of nuclear proteins (Von
413 Hippel & Berg, 1989),
414
415 By slow-tracking, two chromatin-associated populations, 'stable-binding' and 'transient-
416 binding', were observed for all six remodelers. Previous SMT studies on the mammalian
417 Sox2 and yeast Ace1 transcription factors showed that stable-binding subpopulation
418 represent interactions with cognate target sequences (Chen et al., 2014; Mehta et al.,
419 2018). Comparable to reported values for the Rsc2 subunit of RSC and the yeast
420 transcription factors, Ace1 and Gal4 (Donovan et al., 2019; Mehta et al., 2018), all imaged
421 remodelers show stable and transient residence times of 4-7 s and 0.4-0.7 s, respectively.
422 Furthermore, the effect of mutating the DNA-binding domain of CHD1 monomer (Ryan,
423 Sundaramoorthy, Martin, Singh, & Owen-Hughes, 2011; Tran, Steger, Iyer, & Johnson,
424 2000) results in a 3-fold reduction in the τ_{sb} value (from 7.2 $\pm$ 3.3 to 2.4 $\pm$ 0.7 s) (Figure 7-
425 figure supplement 1C,D). Unlike sequence-specific transcription factors, a complete loss
426 of stable-binding would not be expected for remodeling complexes, whose recruitment
427 relies on multiple interactions with gene-specific transcription factors, histone modification
428 recognition domains, and interaction with components of the transcription machinery
429 (Becker & Workman, 2013). Indeed, we speculate that the multiplicity of interaction motifs
430 has a central role in the unusual diffusive behaviors shown by chromatin remodelers.
431
432 Importantly, the fast dissociation rates of remodelers are facilitated by ATP hydrolysis.
433 Five tested ATPase-dead mutants (for ISW2, ISW1, CHD1) show two-fold or greater
434 increase in their stable-binding residence times (Figure 5C-F), highlighting a new role of
435 for ATP-utilization in coupling nucleosome remodeling to rapid enzyme dissociation from
436 chromatin. This also suggests that their mean residence times can reflect timescales for
437 the diverse reactions performed by remodeling enzymes on chromatin *in vivo*. Assuming
438 that the +1 or -1 nucleosomes and the NDR are the main targets for promoter-acting RSC,
439 SWI/SNF, INO80 and ISW2, their 4-7 s stable residence time would include time for
440 diffusion on the NDR as well as time expended for nucleosome remodeling. Biochemical

441 studies have shown that remodelers undertake small translocation steps with remodeling
442 rates of a few bp/sec (Blosser, Yang, Stone, Narlikar, & Zhuang, 2009; Deindl et al., 2013;
443 Harada et al., 2016; Qiu et al., 2018; Sabantsev, Levendosky, Zhuang, Bowman, & Deindl,
444 2019). For example, with an enzymatic rate of 2 bp/s for ISWI (Blosser et al., 2009), an
445 ISWI stable-binding event would allow octamer sliding by roughly 12 bp, which is within
446 range of *in vivo* nucleosome position changes after conditional inactivation of RSC,
447 SWI/SNF, INO80 and ISW2 (Ganguli et al., 2014; Kubik et al., 2019).
448
449 Under our imaging conditions, the chromatin-bound populations of the six remodelers
450 exhibit higher mobility than H2B measured for bulk incorporated histones (Figure 6A-C).
451 We further showed that this enhanced mobility is dependent on the ATPase domain.
452 Mutations in the ISW1, ISW2, and CHD1 Walker A motif implicated in nucleotide binding
453 (Singleton et al., 2007) substantially decreases in vivo mobility. Further analysis of
454 mutations in the CHD1 and ISW2 Walker B motif, implicated in ATP hydrolysis [but not
455 ATP binding] (Singleton et al., 2007), displays a milder decrease of its chromatin mobility,
456 suggesting that nucleotide binding is largely sufficient for promoting diffusion for the two
457 remodelers. Previous observations for other DNA-binding ATPase enzymes have noted
458 ATP binding-dependent, hydrolysis-independent 1D diffusion or sliding on DNA (Cho et
459 al., 2012; Mazur, Mendillo, & Kolodner, 2006; Tóth, Bollins, & Szczelkun, 2015),
460 suggesting that this mode of diffusion to enhance target search may be shared among
461 remodelers. In addition, RSC and Drosophila ISWI remodelers undergo ATP hydrolysis-
462 dependent translocation on ssDNA and dsDNA in vitro (Saha, Wittmeyer, & Cairns, 2005;
463 Whitehouse, Stockdale, Flaus, Szczelkun, & Owen-Hughes, 2003), with processivities of
464 20-70 bp/translocation event (Fischer, Saha, & Cairns, 2007; Saha et al., 2005; Sirinakis
465 et al., 2011; Whitehouse et al., 2003). Finally, the absence of any change in ISW1
466 chromatin-bound mobility upon treatment with a general transcription inhibitor thiolutin
467 rules out transcription *per* se as a source of enhanced remodeler diffusion (Figure 6-figure
468 supplement 1B). In all, our results suggest that chromatin remodelers use the catalytic
469 ATPase not only for nucleosome remodeling but also to enhance target search kinetics
470 by promoting 1D diffusion on chromatin and rapid detachment after reaction.
471

472 Yeast promoter regions can be classified into different groups enriched either for no
473 remodeler or a combination of RSC, SWI/SNF, INO80 and ISW2, with about half of
474 promoters genome-wide harboring at least two distinct remodelers that harbor
475 nucleosome pushing and pulling activities relative to the NDR (Kubik et al., 2019). At
476 promoter regions where opposing remodelers bind, we expect a consecutive "tug-of-war"
477 between the pushing and pulling activities, in which successive engagements would
478 ultimately result in fine-tuning the steady-state nucleosome position, with the final
479 outcome dependent on remodeler occupancy and nucleosome remodeling activity.
480 Based on occupancy estimates, two remodelers may be found to simultaneously engage
481 promoter chromatin (Figure 7C, Figure 7-figure supplement 1A,B), but steric
482 considerations likely preclude two remodelers binding to the same nucleosome or the
483 same face of a nucleosome. Alternatively, at promoter regions where none or only one
484 remodeler binds, other mechanisms are likely to have more substantial roles in
485 nucleosome positioning. These include the sequence-dependent bendability of promoter
486 DNA as well as the binding of general regulatory factors (GRFs), such as Reb1, Abf1,
487 and Rap1, acting as barriers to nucleosome mobility (Struhl & Segal, 2013).
488

489 ***A temporal model for nucleosome remodeling at NDRs***

490 By integrating our live-cell SMT measurements with available genome-wide localization
491 and protein expression data, we estimate temporal occupancies ranging from 11 $\pm$ 5.0 to
492 93 $\pm$ 41% for RSC, SWI/SNF, INO80, and ISW2 at target promoter regions including the
493 NDR and flanking nucleosomes. Our findings of highly dynamic and frequent remodeler-
494 nucleosome interactions are consistent with recent genomics studies showing substantial
495 changes in nucleosome positions upon rapid, conditional inactivation of remodelers in
496 yeast and mammalian systems (Iurlaro et al., 2021; Klein-Brill et al., 2019; Kubik et al.,
497 2019; Schick et al., 2021). Accordingly, we envision a 'nucleosome remodeling cycle' in
498 which remodeler combinations undergo frequent association, ATP-dependent
499 mobilization and dissociation from chromatin to dynamically fine-tune -1 and +1
500 nucleosome positions.
501

502 At the subset of genes targeted by RSC and INO80, we anticipate stochastic recruitment
503 e.g. of RSC (Figure 8). RSC recognizes general promoter characteristics, such as the
504 long DNA stretch of the NDR (Wagner et al., 2020), histone acetylation marks potentially
505 read by 8 bromodomains in four RSC subunits (Josling, Selvarajah, Petter, & Duffy, 2012),
506 and the Rsc3 DNA-binding sequence motif found in several hundred promoters (Badis et
507 al., 2008). Upon binding within the accessible NDR, RSC undergoes 1-D diffusion in an
508 ATP-dependent manner, manifesting higher chromatin-associated mobility. On
509 engagement with either flanking nucleosome substrate [+1 nucleosome shown], RSC
510 uses the energy of ATP hydrolysis to reposition the nucleosome away from NDR,
511 enlarging NDR length. Importantly, this remodeling activity facilitates RSC dissociation.
512 Subsequent stochastic recruitment of INO80, ATP-dependent 1-D diffusion, and
513 nucleosome engagement remodels the nucleosome to move in the opposing direction
514 and narrow the NDR, coupled with INO80 dissociation. Cycles of sequential or
515 simultaneous binding and activity by RSC and INO80 provides a dynamic temporal
516 window of accessibility for promoter chromatin. A similar tug-of-war is anticipated for other
517 combinations of opposing remodelers.
518
519 In a related study (Nguyen et al., 2020), the average promoter occupancy of the yeast
520 PIC that forms upstream and overlapping the +1 nucleosome was found to be in the range
521 of 10%, i.e. on the same order of magnitude but lower than three of four remodelers
522 examined. Similar to chromatin remodelers, a full PIC lasts only several seconds before
523 dissociation from chromatin, but the average promoter is vacant for ~100 seconds before
524 PIC reformation. Thus, we suggest that there may be robust and dynamic competition
525 between PIC components and mobilized NDR-flanking nucleosomes with chromatin
526 exposure of key promoter elements such as the TATA box occurring for only a limited
527 time window allowing proper assembly of downstream PIC components. This temporally
528 positioned +1 nucleosome would enable Pol II to scan and start transcription at the proper,
529 canonical TSS. In this way, the dynamic interactions of remodeling enzymes with their
530 promoter targets provides a temporal, chromatin accessibility-based regulatory
531 mechanism for eukaryotic transcription.
532

533 Taken together, our SMT study elucidates the dynamic behaviors of this family of nuclear
534 proteins and offers insights into additional kinetic functions for the remodeling ATPase
535 and the timescales that govern nucleosome repositioning in relation to transcription
536 events. Outstanding questions for future studies include determining the kinetic
537 parameters for other chromatin regulators such as histone acetyltransferases,
538 methyltransferases, histone de-modification enzymes, and histone chaperones, to gain a
539 comprehensive view of the overall competition for engagement of promoter-proximal
540 nucleosomes, their effects on nucleosome positioning and the dynamics of transcription
541 complexes. Our findings in live cells provide a temporal framework for further testing of
542 proposed models and should facilitate development of in vitro single-molecule assays that
543 allow direct observation of physical and functional interactions between transcription
544 regulators, chromatin, and the transcription machinery.
545
546 **METHODS**
547 **Yeast strains**
548 All *Saccharomyces cerevisiae* strains used in this study are isogenic derivatives of W303
549 strain carrying *pdr5⊿* for efficient JF ligand labeling, and are listed in Supplementary file
550 1. HaloTag was fused to the C-terminus of the protein of interest using standard methods
551 for yeast transformation, using pBS-SK-Halo-NatMX plasmid (Ranjan et al., 2020). Point
552 mutations were introduced by either the traditional "pop-in pop-out" (Rothstein, 1991) or
553 the "50:50" method (Horecka & Davis, 2014), using pUG72 plasmid (P30117, Euroscarf,
554 Germany), and list of primers are provided in Supplementary file 2.
555
556 **Yeast Growth Assays**
557 The cell growth of strains carrying HaloTag fusion constructs were compared to their
558 derived parental genotype. The strains grown to saturation in YPAD (Yeast Extract-
559 Peptone-Dextrose + 40 mg/L Ade-SO_4) were serially diluted (5-fold dilutions) on YPAD
560 plates. Plates were imaged after 48 or 72 h growing at 3 different temperatures (25°C,
561 30°C, and 38°C).
562
563 **Cell Lysate Preparation to check integrity of HaloTag fusion proteins**

564 Yeast cultures growing at early log phase (OD600 0.2) were treated with JF646 dye at a
565 saturating dye concentration of 20 nM JF646 (Grimm et al., 2015) was used instead of
566 JF552 for better dye labeling (Ranjan et al., 2020). The cell extract was prepared using
567 the NaOH method (Cold Spring Harbor Protocols). Total protein concentration was
568 measured using the Bradford Assay, and 45 ng of total protein was loaded per well in
569 SDS-PAGE. Gels were imaged on Tecan 5 scanner, with Cy5 excitation. After imaging,
570 gels were stained with Coomassie dye for loading control.
571
572 **Yeast culture preparation for single molecule imaging**
573 Yeast cultures growing in CSM+Ade (complete synthetic media) were treated with dyes
574 at early log phase (D600 0.2 - 0.3) for 2 h. For fast-tracking, saturating dye concentrations
575 ranging from 10 to 20 nM JF552 (Zheng et al., 2019) were used depending on factor
576 abundance. For slow-tracking, we used 5 - 7.5 nM JF552. In some instances, we also
577 added JF646 (~5 nM) to visualize nuclear fluorescence without JF552 excitation and to
578 partially reduce JF552 labelling. Cells growing in CSM+Ade medium were harvested
579 around mid-log phase by brief centrifugation (3500 rpm for 2 min), washed at least 3 times,
580 and finally resuspended in CSM medium. Resuspended cells were loaded on
581 Concanavalin A-treated coverslip (#1.5 Micro Coverglass -25 mm Diameter, Electron
582 Microscopy Sciences, Cat. No. 72225-01) assembled on imaging cell chamber (Invitrogen,
583 Cat. No. A7816), where coverslips were flamed prior to the treatment in order to reduce
584 single-to-noise background. After 5 min incubation time, the immobilized cells were
585 further washed 3-5 times with a final resuspension in 1 mL CSM.
586
587 **Live cell, single molecule imaging using wide-field microscopy**
588 *Microscope setup:* All yeast imaging was performed using a custom-built Zeiss widefield
589 microscope (Axio Observer Z1) with a 150X glycerin immersion objective (NA 1.35) as
590 previously described (Ranjan et al., 2020). Data was acquired with EM-CCD (Hamamatsu
591 C9100-13) camera with FF01-750/SP and NF03-405/488/561/635E quad-notch filters for
592 a final x-y pixel size of 107 nm. All imaging was performed with a single excitation channel.
593 For JF552 dye excitation, 555 nm laser (Crystalaser) at (TTL pulsed) with 561 beam-
594 splitter and 612/69 nm filter was used. For JF646 dye excitation, a 639 nm laser with 648

595 beamsplitter and 676/29 nm filter was used. Microscope manipulations (i.e. Z-focus, X/Y
596 translation, filter cube switch) was performed by Zen software (Zeiss, Germany) and
597 camera and data acquisition was controlled by HCImage software (Hamamatsu
598 Photonics, Japan).
599
600 **Data acquisition**
601 After yeast immobilization on the coverslip, cells were imaged for around 2 h at room
602 temperature.
603 *Fast tracking*: 10 ms frame-rate movies were recorded with continuous 555 nm laser
604 irradiation at ~1 kW/cm^2. A field of view of 128 x 128 pixels was used to capture 4-6 yeast
605 nuclei. About 40 movies each lasting about 1.5 min were acquired per imaging session,
606 and at least 2 biological replicates were obtained for each sample.
607 *Slow tracking:* 250 ms frame-rate movies were acquired using continuous 555 nm laser
608 irradiation at 0.05 kW/cm^2 for sufficient signal-to-noise while minimizing photobleaching.
609 A focal plane of 256 x 256 pixels was used to capture 15-20 yeast nuclei. In the beginning
610 of each movie, the 639 nm excitation channel was briefly used to fine-tune the focus, and
611 then immediately switched to 555 nm excitation to start data acquisition. Around 15-20
612 movies were taken per imaging session, with each movie lasting typically 7-9 min. At least
613 2 biological replicates were obtained for each sample.
614
615 **Single molecule image analysis**
616 For each raw movie, we first manually selected a 'substack' where ~1 single molecule per
617 nucleus per frame was observed in order to minimize tracking errors resulting from
618 connecting different molecules as one trajectory. Substack lengths of 5000 frames (50 s)
619 and 750 frames (3.125 min) were selected for fast and slow tracking movies, respectively,
620 using ImageJ (1.52p) custom-written script. The substacks were then applied to the
621 Diatrack software (ver. 3.05) to localize and track single particles(Vallotton & Olivier,
622 2013). For localization, the following parameters were applied: Remove dim: 75 - 85,
623 Remove blurred: 0.1, Activate High Precision mode: ON (HWHM=1 pixel). For tracking,
624 we used max jump of '6' (642 nm) and '3' pixels (321 nm) for fast and slow tracking
625 datasets, respectively. Furthermore, we masked the nuclear regions based on the

maximum intensity Z-projection of the selected substacks to filter out trajectories found outside of the nucleus in the subsequent analysis steps. The Diatrack output file containing information about the x, y coordinate and frame number were then applied for further downstream analysis.

Fast tracking:

MSD-based diffusion coefficient histograms: All "masked" trajectories with at least 5 displacements were analyzed, using the lab custom-written R package, Sojourner (https://rdrr.io/github/sheng-liu/sojourner/). Briefly, for each trajectory, MSD plot for time lags from 2 to 5 Δt (Δt = 10 ms) were generated, then fit to linear regression (filtering out $R^2 < 0.8$ plots). From the slope, the diffusion coefficient was calculated as (where d is the number of dimensions, or 2):

$$D = 2d\frac{MSD}{dt}$$

Spot-On (Hansen et al., 2018): All "masked" trajectories with at least 2 displacements were analyzed. The following parameters were applied for Jump Length Distribution: Bin width (μm): 0.01, Number of time-points: 6, Jumps to consider: 4, Use entire trajectories No, Max jump (μm): 2. Additionally, the following parameters were applied for 2-state Model Fitting: D_{bound} ($\mu m^2/s$): 0.0005-0.1, D_{free} ($\mu m^2/s$): 0.15-25, F_{bound}: 0-1, Localization error (μm): Fit from data (0.01-0.1), dZ (μm): 0.6, Use Z correction, Model Fit: CDF, Iterations: 3.

vbSPT (variational Bayesian) HMM (Persson et al., 2013): All "masked" trajectories with at least 2 displacements were analyzed. The following parameters were used to run vbSPT-1.1.3 to classify each displacement into two states, "Bound" or "Free" (Hansen *et al.*, 2020, https://gitlab.com/anders.sejr.hansen/anisotropy): timestep= 0.01; dim= 2; trjLmin= 2; runs= 3; maxHidden= 2; stateEstimate= 1; bootstrapNum=10; fullBootstrap= 0; init_D = [0.001, 16]; init_tD = [2, 20]*timestep; and default prior choices according to (Persson et al., 2013).

Then each trajectory was sub-classified as “Bound only” if all displacements are classified as bound state; “Free only” if all displacements are classified as free state; and “Transitioning” if the trajectory contains both bound and free displacements with at least two consecutive displacements in each state. To validate that the transitioning trajectories consist of bound and free states, we calculated and compared the displacement length between “bound only” and bound segments of transitioning trajectories, and between “free only” and free segments of transitioning trajectories. Finally, the sub-classified trajectories were used to regenerate the diffusion coefficient histograms.

Radius of confinement: All “masked” trajectories with at least 4 displacements were analyzed, as described previously (Lerner et al., 2020). To determine the radius of confinement exhibited by chromatin-bound molecules, we analyzed trajectories classified as “bound only” by vbSPT (as described above). Since many confined trajectories with low D do not pass the $R^2 \geq 0.8$ filter, we used all trajectories whose MSD plots passed the more lenient $R^2 \geq 0.1$ filtering. The MSD plot was then fit to the circular confined diffusion model:

$$MSD_{circle} = R^2 \cdot \left(1 - e^{\frac{-4 \cdot D \cdot t_{lag}}{R^2}}\right)$$

where R is the radius of confinement, D is the short-term diffusion coefficient. Specifically, the first 10 time points of the MSD plot were used to fit to the model, and trajectories with squared norm of residual (RSS) higher than 10^{-5} and Rc higher than 300 nm were discarded.

Slow tracking:

Residence times: Using Sojourner package, the apparent lifetimes (temporal length of trajectories) were determined for all “masked” trajectories lasting at least 3 frames. To account for blinking or mislocalizations, we allowed for gaps up to 2 frames between two localizations and linked them as one trajectory if they were less than 3 pixels apart. 1-CDF curves were generated and fit to a double exponential decay model:

$$P(t) = f_{sb}\, e^{-k_{sb}t} + f_{tb}\, e^{-k_{tb}t}$$

where k_{sb} and k_{tb} correspond to dissociation rates for stable- and transient-binding events, respectively, and $1 = f_{sb} + f_{tb}$ for the 2 components.

The apparent k_{sb} and k_{tb} values are affected by technical and imaging limitations such as photobleaching and chromatin movements. To correct for this bias, we used apparent dissociation rates of H2B imaged under same conditions as described previously(Hansen et al., 2017). The corrected residence times for stable- (τ_{sb}) and transient binding (τ_{tb}) were calculated as follows:

$$\tau_{sb} = \frac{1}{k_{sb} - k_{sb,H2B}}$$

$$\tau_{tb} = \frac{1}{k_{tb} - k_{sb,H2B}}$$

Apparent diffusion coefficient values for stably bound trajectories: All "masked" trajectories lasting at least 5 frames (not allowing for gaps) were analyzed, using Sojourner package. For each trajectory, MSD plot for time lags from 2 to 5 Δt (Δt = 10 ms) were generated, then fit to linear regression (filtering out $R^2 < 0.8$ plots). From the slope, the diffusion coefficient was calculated as (where d is the number of dimensions, or 2):

$$D = 2d\frac{MSD}{dt}$$

Occupancy calculation

To calculate temporal occupancy, we integrated approaches from previous studies (Chen et al., 2014; Loffreda et al., 2017; Tatavosian et al., 2018).

Search time (τ_{search}) is the average time it takes for a molecule to go from one specific site to its next specific site. The two specific binding events (lasting for τ_{sb}) are interspersed by a number of trials (N_{trials}) binding to non-specific sites (lasting for τ_{tb}). τ_{free} is the average free time between 2 binding events. Assuming equal probability of binding to all specific and non-specific sites, the search time is calculated as follows:

$$\tau_{search} = N_{trials} \times \tau_{tb} + (N_{trials} + 1) \times \tau_{free}$$

N_{trials} depends on the ratio of number of non-specific (N_{ns}) to specific sites (N_s), or r_s:

$$N_{trials} = \frac{N_s + N_{ns}}{N_s} = 1 + r_s$$

Here, r_s can be determined based on two assumed scenarios for bound molecules observed during slow tracking (as described in Nguyen et al. 2020). First, f_{sb} determined by slow tracking depends on the time a molecule spends bound to specific sites compared to nonspecific sites:

$$f_{sb} = \frac{N_s \times \tau_{sb}}{N_s \times \tau_{sb} + N_{ns} \times \tau_{tb}} = \frac{\tau_{sb}}{\tau_{sb} + r_{s,1} \times \tau_{tb}}$$

Thus r_s is equal to:

$$r_{s,1} = \frac{\tau_{sb}}{\tau_{tb}} \times (\frac{1}{f_{sb}} - 1)$$

In the second scenario, f_{sb} depends on the probability that a free molecule binds to a specific site over all sites:

$$f_{sb} = \frac{N_s}{N_s + N_{ns}} = \frac{1}{1 + r_{s,2}}$$

In this case r_s is:

$$r_{s,2} = \frac{1}{f_{sb}} - 1$$

We take the average value calculated from the 2 proposed scenarios to finally determine r_s:

$$r_s = \frac{1}{2}(\frac{1}{f_{sb}} - 1)(\frac{\tau_{sb}}{\tau_{tb}} + 1)$$

In fast tracking, F_{bound} is percentage or fraction of the time a molecule spends bound to chromatin either specifically or non-specifically:

$$F_{bound} = \frac{N_{trials} \times \tau_{tb} + \tau_{sb}}{N_{trials} \times \tau_{tb} + \tau_{sb} + (N_{trials} + 1) \times \tau_{free}}$$

Thus τ_{free} is (in terms of r_s):

$$\tau_{free} = \frac{\frac{(1 + r_s) \times \tau_{tb} + \tau_{sb}}{F_{bound}} - (1 + r_s) \times \tau_{tb} - \tau_{sb}}{2 + r_s}$$

Using the values derived for r_s and τ_{free}, we then calculated the search time as shown above.

Sampling interval (SI) is the time interval between two specific binding events at a given site as described previously (Chen et al., 2014):

$$Sampling\ Interval\ (SI) = \frac{(\tau_{search} + \tau_{sb}) \times N_{targets}}{N_{molecules}}$$

We used $N_{targets}$ values presented by (Kubik et al., 2019). $N_{molecules}$ was determined as the median and standard error values (Ho et al., 2018), and their standard error was used for error propagation.

Finally, occupancy is the temporal probability that a given specific site is occupied by the protein of interest:

$$Occupancy = \frac{\tau_{sb}}{SI}$$

Target occupancy simulation

Remodeler occupancy at a target promoter region was simulated as described previously (Nguyen et al. 2020). Briefly, experimentally determined τ_{sb} and estimated sampling interval (SI) values were used to simulate sequential promoter-occupied and vacant states over the time trace (500 s). The duration for each occupied and vacant state was randomly chosen from exponential distributions of the average τ_{sb} and (SI- τ_{sb}) values, respectively. For promoter regions targeted by multiple remodelers, each remodeler was independently subject to the occupancy simulation, and the number of any single or multiple remodeler(s) co-occupying each timepoint was calculated throughout the time trace.

ACKNOWLEDGEMENTS

We thank Vu Q. Nguyen, Anand Ranjan, and Gaku Mizuguchi for experimental guidance at the initial stages of this project, Sun Jay Yoo, Yick Hin Ling and Taibo Li for computational assistance, Pascal Vallotton for support with Diatrack software, Jonathan Lerner, Ken Zaret, and Melike Lakadamyali for assistance with the Two-parameter single-molecule analysis, Slawomir Kubik and David Shore for advice on analysis of genomic data on remodeling enzymes, Toshio Tsukiyama and Brad Cairns for yeast strains, Anders Hansen and Greg Bowman for discussions and Wu lab members for helpful comments. This study was supported by funds from a Korean Foundation for Advanced

768 Studies Fellowship (J.M.K.), a Johns Hopkins Bloomberg Distinguished Professorship
769 (C.W.) and National Institute of Health grant GM132290-01 (C.W.).
770

771 **AUTHOR CONTRIBUTIONS**

772 Conceptualization, J.M.K. and C.W.; Software, S.L., X.T., J.M.K., and T.L.; Investigation,
773 J.M.K., P.V., V.J., K.Y.L., and J.S.; Formal Analysis, J.M.K., P.V., and V.J.; Writing –
774 Original Draft, J.M.K. and C.W.; Writing – Review & Editing, J.M.K and C.W.; Funding
775 Acquisition, C.W.; Resources, Q.Z. and L.D.L.; Supervision, J.M.K. and C.W.
776

777 **COMPETING INTERESTS**

778 T.L. holds intellectual property rights related to Janelia Fluor dyes used in this publication.
779 L.D.L. and Q.Z. are listed as inventors on patents and patent applications whose value
780 might be affected by publication. The remaining authors declare no competing interests.
781

782 **REFERENCES**

783 Albert, I., Mavrich, T. N., Tomsho, L. P., Qi, J., Zanton, S. J., Schuster, S. C., & Pugh,
784 B. F. (2007). Translational and rotational settings of H2A.Z nucleosomes across the
785 Saccharomyces cerevisiae genome. *Nature*. https://doi.org/10.1038/nature05632
786 Almer, A., & Hörz, W. (1986). Nuclease hypersensitive regions with adjacent positioned
787 nucleosomes mark the gene boundaries of the PHO5/PHO3 locus in yeast. *The*
788 *EMBO Journal*, *5*(10), 2681–2687. https://doi.org/10.1002/j.1460-
789 2075.1986.tb04551.x
790 Badis, G., Chan, E. T., van Bakel, H., Pena-Castillo, L., Tillo, D., Tsui, K., … Hughes, T.
791 R. (2008). A Library of Yeast Transcription Factor Motifs Reveals a Widespread
792 Function for Rsc3 in Targeting Nucleosome Exclusion at Promoters. *Molecular Cell*,
793 *32*(6), 878–887. https://doi.org/10.1016/j.molcel.2008.11.020
794 Ball, D. A., Mehta, G. D., Salomon-Kent, R., Mazza, D., Morisaki, T., Mueller, F., …
795 Karpova, T. S. (2016). Single molecule tracking of Ace1p in Saccharomyces
796 cerevisiae defines a characteristic residence time for non-specific interactions of
797 transcription factors with chromatin. *Nucleic Acids Research*, *44*(21), 1–12.
798 https://doi.org/10.1093/nar/gkw744

799 Basu, S., Shukron, O., Ponjavic, A., Parruto, P., Boucher, W., Zhang, W., … Laue, E. D.
800 (2020). Live-cell 3D single-molecule tracking reveals how NuRD modulates
801 enhancer dynamics. *BioRxiv*, 2020.04.03.003178.
802 https://doi.org/10.1101/2020.04.03.003178
803 Becker, P. B., & Workman, J. L. (2013). Nucleosome remodeling and epigenetics. *Cold*
804 *Spring Harbor Perspectives in Biology*.
805 https://doi.org/10.1101/cshperspect.a017905
806 Blosser, T. R., Yang, J. G., Stone, M. D., Narlikar, G. J., & Zhuang, X. (2009). Dynamics
807 of nucleosome remodelling by individual ACF complexes. *Nature*, *462*(7276),
808 1022–1027. https://doi.org/10.1038/nature08627
809 Brahma, S., & Henikoff, S. (2019). RSC-Associated Subnucleosomes Define MNase-
810 Sensitive Promoters in Yeast. *Molecular Cell*.
811 https://doi.org/10.1016/j.molcel.2018.10.046
812 Chen, J., Zhang, Z., Li, L., Chen, B. C., Revyakin, A., Hajj, B., … Liu, Z. (2014). Single-
813 molecule dynamics of enhanceosome assembly in embryonic stem cells. *Cell*.
814 https://doi.org/10.1016/j.cell.2014.01.062
815 Cheung, V., Chua, G., Batada, N. N., Landry, C. R., Michnick, S. W., Hughes, T. R., &
816 Winston, F. (2008). Chromatin- and transcription-related factors repress
817 transcription from within coding regions throughout the Saccharomyces cerevisiae
818 genome. *PLoS Biology*. https://doi.org/10.1371/journal.pbio.0060277
819 Cho, W. K., Jeong, C., Kim, D., Chang, M., Song, K. M., Hanne, J., … Lee, J. B. (2012).
820 ATP alters the diffusion mechanics of MutS on mismatched DNA. *Structure*.
821 https://doi.org/10.1016/j.str.2012.04.017
822 Cutler, S., Lee, L. J., & Tsukiyama, T. (2018). Chromatin remodeling factors isw2 and
823 ino80 regulate chromatin, replication, and copy number of the saccharomyces
824 cerevisiae ribosomal DNA locus. *Genetics*.
825 https://doi.org/10.1534/genetics.118.301579
826 Deindl, S., Hwang, W. L., Hota, S. K., Blosser, T. R., Prasad, P., Bartholomew, B., &
827 Zhuang, X. (2013). ISWI remodelers slide nucleosomes with coordinated multi-
828 base-pair entry steps and single-base-pair exit steps. *Cell*, *152*(3), 442–452.
829 https://doi.org/10.1016/j.cell.2012.12.040

830 Donovan, B. T., Huynh, A., Ball, D. A., Patel, H. P., Poirier, M. G., Larson, D. R., …
831 Lenstra, T. L. (2019). Live-cell imaging reveals the interplay between transcription
832 factors, nucleosomes, and bursting. *The EMBO Journal*.
833 https://doi.org/10.15252/embj.2018100809
834 Erdel, F., Schubert, T., Marth, C., Längst, G., & Rippe, K. (2010). Human ISWI
835 chromatin-remodeling complexes sample nucleosomes via transient binding
836 reactions and become immobilized at active sites. *Proceedings of the National*
837 *Academy of Sciences of the United States of America*.
838 https://doi.org/10.1073/pnas.1003438107
839 Fischer, C. J., Saha, A., & Cairns, B. R. (2007). Kinetic model for the ATP-dependent
840 translocation of Saccharomyces cerevisiae RSC along double-stranded DNA.
841 *Biochemistry*. https://doi.org/10.1021/bi700930n
842 Fitzgerald, D. J., DeLuca, C., Berger, I., Gaillard, H., Sigrist, R., Schimmele, K., &
843 Richmond, T. J. (2004). Reaction cycle of the yeast Isw2 chromatin remodeling
844 complex. *EMBO Journal*. https://doi.org/10.1038/sj.emboj.7600364
845 Floer, M., Wang, X., Prabhu, V., Berrozpe, G., Narayan, S., Spagna, D., … Ptashne, M.
846 (2010). A RSC/nucleosome complex determines chromatin architecture and
847 facilitates activator binding. *Cell*. https://doi.org/10.1016/j.cell.2010.03.048
848 Ganguli, D., Chereji, R. V., Iben, J. R., Cole, H. A., & Clark, D. J. (2014). RSC-
849 dependent constructive and destructive interference between opposing arrays of
850 phased nucleosomes in yeast. *Genome Research*.
851 https://doi.org/10.1101/gr.177014.114
852 Gasser, S. M. (2002). Nuclear architecture: Visualizing chromatin dynamics in
853 interphase nuclei. *Science*. https://doi.org/10.1126/science.1067703
854 Gelbart, M. E., Rechsteiner, T., Timothy, J., Tsukiyama, T., & Richmond, T. J. (2001).
855 Interactions of Isw2 Chromatin Remodeling Complex with Nucleosomal Arrays :
856 Analyses Using Recombinant Yeast Histones and Immobilized Templates
857 Interactions of Isw2 Chromatin Remodeling Complex with Nucleosomal Arrays :
858 Analyses Using Recombinant Yeast Hi. *Molecular and Cellular Biology*, (June
859 2014). https://doi.org/10.1128/MCB.21.6.2098
860 Grimm, J. B., English, B. P., Chen, J., Slaughter, J. P., Zhang, Z., Revyakin, A., …

Lavis, L. D. (2015). A general method to improve fluorophores for live-cell and single-molecule microscopy. *Nature Methods*. https://doi.org/10.1038/nmeth.3256

Gu, B., Swigut, T., Spencley, A., Bauer, M. R., Chung, M., Meyer, T., & Wysocka, J. (2018). Transcription-coupled changes in nuclear mobility of mammalian cis-regulatory elements. *Science*. https://doi.org/10.1126/science.aao3136

Hansen, A. S., Amitai, A., Cattoglio, C., Tjian, R., & Darzacq, X. (2020). Guided nuclear exploration increases CTCF target search efficiency. *Nature Chemical Biology*, *16*(3), 257–266. https://doi.org/10.1038/s41589-019-0422-3

Hansen, A. S., Pustova, I., Cattoglio, C., Tjian, R., & Darzacq, X. (2017). CTCF and cohesin regulate chromatin loop stability with distinct dynamics. *ELife*, *6*. https://doi.org/10.7554/eLife.25776.001

Hansen, A. S., Woringer, M., Grimm, J. B., Lavis, L. D., Tjian, R., & Darzacq, X. (2018). Robust model-based analysis of single-particle tracking experiments with spot-on. *ELife*. https://doi.org/10.7554/eLife.33125

Harada, B. T., Hwang, W. L., Deindl, S., Chatterjee, N., Bartholomew, B., & Zhuang, X. (2016). Stepwise nucleosome translocation by RSC remodeling complexes. *ELife*, *5*(FEBRUARY2016), 1–20. https://doi.org/10.7554/eLife.10051

Hartley, P. D., & Madhani, H. D. (2009). Mechanisms that Specify Promoter Nucleosome Location and Identity. *Cell*. https://doi.org/10.1016/j.cell.2009.02.043

Hauk, G., McKnight, J. N., Nodelman, I. M., & Bowman, G. D. (2010). The Chromodomains of the Chd1 Chromatin Remodeler Regulate DNA Access to the ATPase Motor. *Molecular Cell*. https://doi.org/10.1016/j.molcel.2010.08.012

Heintzman, N. D., Stuart, R. K., Hon, G., Fu, Y., Ching, C. W., Hawkins, R. D., … Ren, B. (2007). Distinct and predictive chromatin signatures of transcriptional promoters and enhancers in the human genome. *Nature Genetics*. https://doi.org/10.1038/ng1966

Ho, B., Baryshnikova, A., & Brown, G. W. (2018). Unification of Protein Abundance Datasets Yields a Quantitative Saccharomyces cerevisiae Proteome. *Cell Systems*. https://doi.org/10.1016/j.cels.2017.12.004

Horecka, J., & Davis, R. W. (2014). The 50:50 method for PCR-based seamless genome editing in yeast. *Yeast (Chichester, England)*.

https://doi.org/10.1002/yea.2992

Iurlaro, M., Stadler, M. B., Masoni, F., Jagani, Z., Galli, G. G., & Schübeler, D. (2021). Mammalian SWI/SNF continuously restores local accessibility to chromatin. *Nature Genetics*. https://doi.org/10.1038/s41588-020-00768-w

Izeddin, I., Récamier, V., Bosanac, L., Cissé, I. I., Boudarene, L., Dugast-Darzacq, C., … Darzacq, X. (2014). Single-molecule tracking in live cells reveals distinct target-search strategies of transcription factors in the nucleus. *ELife*, *2014*(3), 1–27. https://doi.org/10.7554/eLife.02230

Josling, G. A., Selvarajah, S. A., Petter, M., & Duffy, M. F. (2012). The role of bromodomain proteins in regulating gene expression. *Genes*, *3*(2), 320–343. https://doi.org/10.3390/genes3020320

Klein-Brill, A., Joseph-Strauss, D., Appleboim, A., & Friedman, N. (2019). Dynamics of Chromatin and Transcription during Transient Depletion of the RSC Chromatin Remodeling Complex. *Cell Reports*. https://doi.org/10.1016/j.celrep.2018.12.020

Kubik, S., Bruzzone, M. J., Challal, D., Dreos, R., Mattarocci, S., Bucher, P., … Shore, D. (2019). Opposing chromatin remodelers control transcription initiation frequency and start site selection. *Nature Structural and Molecular Biology*. https://doi.org/10.1038/s41594-019-0273-3

Kubik, S., Bruzzone, M. J., Jacquet, P., Falcone, J. L., Rougemont, J., & Shore, D. (2015). Nucleosome Stability Distinguishes Two Different Promoter Types at All Protein-Coding Genes in Yeast. *Molecular Cell*. https://doi.org/10.1016/j.molcel.2015.10.002

Kubik, S., O'Duibhir, E., de Jonge, W. J., Mattarocci, S., Albert, B., Falcone, J. L., … Shore, D. (2018). Sequence-Directed Action of RSC Remodeler and General Regulatory Factors Modulates +1 Nucleosome Position to Facilitate Transcription. *Molecular Cell*. https://doi.org/10.1016/j.molcel.2018.05.030

Lai, W. K. M., & Pugh, B. F. (2017a). Understanding nucleosome dynamics and their links to gene expression and DNA replication. *Nature Reviews Molecular Cell Biology*. https://doi.org/10.1038/nrm.2017.47

Lai, W. K. M., & Pugh, B. F. (2017b). Understanding nucleosome dynamics and their links to gene expression and DNA replication. *Nature Reviews Molecular Cell*

923 *Biology*, *18*(9), 548–562. https://doi.org/10.1038/nrm.2017.47
924 Lerner, J., Gomez-Garcia, P. A., McCarthy, R. L., Liu, Z., Lakadamyali, M., & Zaret, K.
925 S. (2020). Two-Parameter Mobility Assessments Discriminate Diverse Regulatory
926 Factor Behaviors in Chromatin. *Journal of Cleaner Production*.
927 https://doi.org/10.1016/j.molcel.2020.05.036
928 Lionnet, T., & Wu, C. (2021). Single-molecule tracking of transcription protein dynamics
929 in living cells: seeing is believing, but what are we seeing? *Current Opinion in*
930 *Genetics & Development*, *In press*. Retrieved from
931 https://www.journals.elsevier.com/current-opinion-in-genetics-and-development
932 Loffreda, A., Jacchetti, E., Antunes, S., Rainone, P., Daniele, T., Morisaki, T., … Mazza,
933 D. (2017). Live-cell p53 single-molecule binding is modulated by C-terminal
934 acetylation and correlates with transcriptional activity. *Nature Communications*.
935 https://doi.org/10.1038/s41467-017-00398-7
936 Lusser, A., Urwin, D. L., & Kadonaga, J. T. (2005). Distinct activities of CHD1 and ACF
937 in ATP-dependent chromatin assembly. *Nature Structural and Molecular Biology*,
938 *12*(2), 160–166. https://doi.org/10.1038/nsmb884
939 Maier, V. K., Chioda, M., Rhodes, D., & Becker, P. B. (2008). ACF catalyses
940 chromatosome movements in chromatin fibres. *EMBO Journal*.
941 https://doi.org/10.1038/sj.emboj.7601902
942 Marshall, W. F., Straight, A., Marko, J. F., Swedlow, J., Dernburg, A., Belmont, A., …
943 Sedat, J. W. (1997). Interphase chromosomes undergo constrained diffusional
944 motion in living cells. *Current Biology*. https://doi.org/10.1016/S0960-
945 9822(06)00412-X
946 Mavrich, T. N., Ioshikhes, I. P., Venters, B. J., Jiang, C., Tomsho, L. P., Qi, J., … Pugh,
947 B. F. (2008). A barrier nucleosome model for statistical positioning of nucleosomes
948 throughout the yeast genome. *Genome Research*.
949 https://doi.org/10.1101/gr.078261.108
950 Mazur, D. J., Mendillo, M. L., & Kolodner, R. D. (2006). Inhibition of Msh6 ATPase
951 Activity by Mispaired DNA Induces a Msh2(ATP)-Msh6(ATP) State Capable of
952 Hydrolysis-Independent Movement along DNA. *Molecular Cell*.
953 https://doi.org/10.1016/j.molcel.2006.02.010

954 McSwiggen, D., Hansen, A., Marie-Nelly, H., Teves, S., Heckert, A., Dugast-Darzacq,
955 C., … Darzacq, X. (2018). Transient DNA Binding Induces RNA Polymerase II
956 Compartmentalization During Herpesviral Infection Distinct From Phase
957 Separation. *BioRxiv*. https://doi.org/10.1101/375071
958 Mehta, G. D., Ball, D. A., Eriksson, P. R., Chereji, R. V., Clark, D. J., McNally, J. G., &
959 Karpova, T. S. (2018). Single-Molecule Analysis Reveals Linked Cycles of RSC
960 Chromatin Remodeling and Ace1p Transcription Factor Binding in Yeast. *Molecular*
961 *Cell*. https://doi.org/10.1016/j.molcel.2018.09.009
962 Morillon, A., Karabetsou, N., O'Sullivan, J., Kent, N., Proudfoot, N., & Mellor, J. (2003).
963 Isw1 Chromatin Remodeling ATPase Coordinates Transcription Elongation and
964 Termination by RNA Polymerase II. *Cell*. https://doi.org/10.1016/S0092-
965 8674(03)00880-8
966 Neumann, F. R., Dion, V., Gehlen, L. R., Tsai-Pflugfelder, M., Schmid, R., Taddei, A., &
967 Gasser, S. M. (2012). Targeted INO80 enhances subnuclear chromatin movement
968 and ectopic homologous recombination. *Genes and Development*.
969 https://doi.org/10.1101/gad.176156.111
970 Ocampo, J., Chereji, R. V., Eriksson, P. R., & Clark, D. J. (2016). The ISW1 and CHD1
971 ATP-dependent chromatin remodelers compete to set nucleosome spacing in vivo.
972 *Nucleic Acids Research*. https://doi.org/10.1093/nar/gkw068
973 Ocampo, J., Chereji, R. V., Eriksson, P. R., & Clark, D. J. (2019). Contrasting roles of
974 the RSC and ISW1/CHD1 chromatin remodelers in RNA polymerase II elongation
975 and termination. *Genome Research*. https://doi.org/10.1101/gr.242032.118
976 Parnell, T. J., Schlichter, A., Wilson, B. G., & Cairns, B. R. (2015). The chromatin
977 remodelers RSC and ISW1 display functional and chromatin-based promoter
978 antagonism. *ELife*. https://doi.org/10.7554/eLife.06073
979 Persson, F., Lindén, M., Unoson, C., & Elf, J. (2013). Extracting intracellular diffusive
980 states and transition rates from single-molecule tracking data. *Nature Methods*.
981 https://doi.org/10.1038/nmeth.2367
982 Prajapati, H. K., Ocampo, J., & Clark, D. J. (2020). Interplay among atp-dependent
983 chromatin remodelers determines chromatin organisation in yeast. *Biology*, *9*(8), 1–
984 23. https://doi.org/10.3390/biology9080190

985 Qiu, Y., Levendosky, R., Chakravarthy, S., Patel, A., Myong, S., States, U., … States,
986 U. (2018). HHS Public Access, *68*(1), 76–88.
987 https://doi.org/10.1016/j.molcel.2017.08.018.The
988 Radman-Livaja, M., Quan, T. K., Valenzuela, L., Armstrong, J. A., van Welsem, T., Kim,
989 T. S., … Hartzog, G. A. (2012). A key role for Chd1 in histone H3 dynamics at the 3′
990 ends of long genes in yeast. *PLoS Genetics*.
991 https://doi.org/10.1371/journal.pgen.1002811
992 Ramachandran, S., Zentner, G. E., & Henikoff, S. (2015). Asymmetric nucleosomes
993 flank promoters in the budding yeast genome. *Genome Research*, *25*(3), 381–390.
994 https://doi.org/10.1101/gr.182618.114
995 Rando, O. J., & Winston, F. (2012). Chromatin and transcription in yeast. *Genetics*.
996 https://doi.org/10.1534/genetics.111.132266
997 Ranjan, A., Nguyen, V. Q., Liu, S., Wisniewski, J., Kim, J. M., Tang, X., … Wu, C.
998 (2020). Live-cell single particle imaging reveals the role of RNA polymerase II in
999 histone H2A.Z eviction. *ELife*. https://doi.org/10.7554/elife.55667
1000 Rossi, M. J., Kuntala, P. K., Lai, W. K. M., Yamada, N., Badjatia, N., Mittal, C., … Pugh,
1001 B. F. (2021). A high-resolution protein architecture of the budding yeast genome.
1002 *Nature*. https://doi.org/10.1038/s41586-021-03314-8
1003 Rothstein, R. (1991). Targeting, Disruption, Replacement, and Allele Rescue:
1004 Integrative DNA Transformation in Yeast. *Methods in Enzymology*.
1005 https://doi.org/10.1016/0076-6879(91)94022-5
1006 Ryan, D. P., Sundaramoorthy, R., Martin, D., Singh, V., & Owen-Hughes, T. (2011). The
1007 DNA-binding domain of the Chd1 chromatin-remodelling enzyme contains SANT
1008 and SLIDE domains. *EMBO Journal*, *30*(13), 2596–2609.
1009 https://doi.org/10.1038/emboj.2011.166
1010 Sabantsev, A., Levendosky, R. F., Zhuang, X., Bowman, G. D., & Deindl, S. (2019).
1011 Direct observation of coordinated DNA movements on the nucleosome during
1012 chromatin remodelling. *Nature Communications*, *10*(1), 1–12.
1013 https://doi.org/10.1038/s41467-019-09657-1
1014 Saha, A., Wittmeyer, J., & Cairns, B. R. (2005). Chromatin remodeling through
1015 directional DNA translocation from an internal nucleosomal site. *Nature Structural*

1016 *and Molecular Biology*, *12*(9), 747–755. https://doi.org/10.1038/nsmb973
1017 Schick, S., Grosche, S., Kohl, K. E., Drpic, D., Jaeger, M. G., Marella, N. C., … Kubicek,
1018 S. (2021). Acute BAF perturbation causes immediate changes in chromatin
1019 accessibility. *Nature Genetics*. https://doi.org/10.1038/s41588-021-00777-3
1020 Shimada, K., Oma, Y., Schleker, T., Kugou, K., Ohta, K., Harata, M., & Gasser, S. M.
1021 (2008). Ino80 Chromatin Remodeling Complex Promotes Recovery of Stalled
1022 Replication Forks. *Current Biology*. https://doi.org/10.1016/j.cub.2008.03.049
1023 Singleton, M. R., Dillingham, M. S., & Wigley, D. B. (2007). Structure and Mechanism of
1024 Helicases and Nucleic Acid Translocases. *Annual Review of Biochemistry*, *76*(1),
1025 23–50. https://doi.org/10.1146/annurev.biochem.76.052305.115300
1026 Sirinakis, G., Clapier, C. R., Gao, Y., Viswanathan, R., Cairns, B. R., & Zhang, Y.
1027 (2011). The RSC chromatin remodelling ATPase translocates DNA with high force
1028 and small step size. *EMBO Journal*, *30*(12), 2364–2372.
1029 https://doi.org/10.1038/emboj.2011.141
1030 Smolle, M., Venkatesh, S., Gogol, M. M., Li, H., Zhang, Y., Florens, L., … Workman, J.
1031 L. (2012a). Chromatin remodelers Isw1 and Chd1 maintain chromatin structure
1032 during transcription by preventing histone exchange. *Nature Structural and*
1033 *Molecular Biology*. https://doi.org/10.1038/nsmb.2312
1034 Smolle, M., Venkatesh, S., Gogol, M. M., Li, H., Zhang, Y., Florens, L., … Workman, J.
1035 L. (2012b). Chromatin remodelers Isw1 and Chd1 maintain chromatin structure
1036 during transcription by preventing histone exchange. *Nature Structural and*
1037 *Molecular Biology*. https://doi.org/10.1038/nsmb.2312
1038 Soutoglou, E., & Misteli, T. (2007). Mobility and immobility of chromatin in transcription
1039 and genome stability. *Current Opinion in Genetics and Development*.
1040 https://doi.org/10.1016/j.gde.2007.08.004
1041 Spain, M. M., Ansari, S. A., Pathak, R., Palumbo, M. J., Morse, R. H., & Govind, C. K.
1042 (2014). The RSC Complex Localizes to Coding Sequences to Regulate Pol II and
1043 Histone Occupancy. *Molecular Cell*. https://doi.org/10.1016/j.molcel.2014.10.002
1044 Strom, A. R., Emelyanov, A. V., Mir, M., Fyodorov, D. V., Darzacq, X., & Karpen, G. H.
1045 (2017). Phase separation drives heterochromatin domain formation. *Nature*.
1046 https://doi.org/10.1038/nature22989

1047 Struhl, K., & Segal, E. (2013). Determinants of nucleosome positioning. *Nature*
1048 *Structural and Molecular Biology*, *20*(3), 267–273.
1049 https://doi.org/10.1038/nsmb.2506
1050 Tatavosian, R., Duc, H. N., Huynh, T. N., Fang, D., Schmitt, B., Shi, X., … Ren, X.
1051 (2018). Live-cell single-molecule dynamics of PcG proteins imposed by the DIPG
1052 H3.3K27M mutation. *Nature Communications*. https://doi.org/10.1038/s41467-018-
1053 04455-7
1054 Tóth, J., Bollins, J., & Szczelkun, M. D. (2015). Re-evaluating the kinetics of ATP
1055 hydrolysis during initiation of DNA sliding by Type III restriction enzymes. *Nucleic*
1056 *Acids Research*. https://doi.org/10.1093/nar/gkv1154
1057 Tran, H. G., Steger, D. J., Iyer, V. R., & Johnson, A. D. (2000). The chrome domain
1058 protein Chd1p from budding yeast is an ATP-dependent chromatin-modifying
1059 factor. *EMBO Journal*. https://doi.org/10.1093/emboj/19.10.2323
1060 Tsukiyama, T., Palmer, J., Landel, C. C., Shiloach, J., & Wu, C. (1999).
1061 Characterization of the imitation switch subfamily of ATP-dependent chromatin-
1062 remodeling factors in Saccharomyces cerevisiae. *Genes and Development*.
1063 https://doi.org/10.1101/gad.13.6.686
1064 Vallotton, P., & Olivier, S. (2013). Tri-track: Free software for large-scale particle
1065 tracking. *Microscopy and Microanalysis*.
1066 https://doi.org/10.1017/S1431927612014328
1067 Vary, J. C., Gangaraju, V. K., Qin, J., Landel, C. C., Kooperberg, C., Bartholomew, B., &
1068 Tsukiyama, T. (2003). Yeast Isw1p forms two separable complexes in vivo.
1069 *Molecular and Cellular Biology*. https://doi.org/10.1128/MCB.23.1.80-91.2003
1070 Von Hippel, P. H., & Berg, O. G. (1989). Facilitated target location in biological systems.
1071 *Journal of Biological Chemistry*.
1072 Wagner, F. R., Dienemann, C., Wang, H., Stützer, A., Tegunov, D., Urlaub, H., &
1073 Cramer, P. (2020). Structure of SWI/SNF chromatin remodeller RSC bound to a
1074 nucleosome. *Nature*. https://doi.org/10.1038/s41586-020-2088-0
1075 Walker, J. E., Saraste, M., Runswick, M. J., & Gay, N. J. (1982). Distantly related
1076 sequences in the alpha- and beta-subunits of ATP synthase, myosin, kinases and
1077 other ATP-requiring enzymes and a common nucleotide binding fold. *The EMBO*

1078 *Journal*. https://doi.org/10.1002/j.1460-2075.1982.tb01276.x
1079 Whitehouse, I., Rando, O. J., Delrow, J., & Tsukiyama, T. (2007). Chromatin
1080 remodelling at promoters suppresses antisense transcription. *Nature*, *450*(7172),
1081 1031–1035. https://doi.org/10.1038/nature06391
1082 Whitehouse, I., Stockdale, C., Flaus, A., Szczelkun, M. D., & Owen-Hughes, T. (2003).
1083 Evidence for DNA Translocation by the ISWI Chromatin-Remodeling Enzyme.
1084 *Molecular and Cellular Biology*. https://doi.org/10.1128/mcb.23.6.1935-1945.2003
1085 Wu, C. (1980). The 5' ends of drosophila heat shock genes in chromatin are
1086 hypersensitive to DNase I. *Nature*. https://doi.org/10.1038/286854a0
1087 Yen, K., Vinayachandran, V., Batta, K., Koerber, R. T., & Pugh, B. F. (2012). Genome-
1088 wide nucleosome specificity and directionality of chromatin remodelers. *Cell*.
1089 https://doi.org/10.1016/j.cell.2012.04.036
1090 Yuan, G.-C., Liu, Y.-J., Dion, M. F., Slack, M. D., Wu, L. F., Altschuler, S. J., & Rando,
1091 O. J. (2005). Genome-scale identification of nucleosome positions in
1092 Saccharomyces cerevisiae. *Nature Methods*. https://doi.org/10.1038/nmeth0805-
1093 567
1094 Zentner, G. E., Tsukiyama, T., & Henikoff, S. (2013). ISWI and CHD Chromatin
1095 Remodelers Bind Promoters but Act in Gene Bodies. *PLoS Genetics*, *9*(2),
1096 e1003317. https://doi.org/10.1371/journal.pgen.1003317
1097 Zhang, Z., Wippo, C. J., Wal, M., Ward, E., Korber, P., & Pugh, B. F. (2011). A packing
1098 mechanism for nucleosome organization reconstituted across a eukaryotic
1099 genome. *Science*. https://doi.org/10.1126/science.1200508
1100 Zheng, Q., Ayala, A. X., Chung, I., Weigel, A. V., Ranjan, A., Falco, N., … Lavis, L. D.
1101 (2019). Rational Design of Fluorogenic and Spontaneously Blinking Labels for
1102 Super-Resolution Imaging. *ACS Central Science*.
1103 https://doi.org/10.1021/acscentsci.9b00676
1104

1105 **FIGURE LEGENDS**

1106 **Figure 1.** Chromatin-binding and chromatin-free fractions of RSC, SWI/SNF, INO80, and
1107 ISW2. Diffusion coefficient histograms show the chromatin-binding fraction is highest for
1108 RSC among gene promoter-acting remodelers. **(A)** Experimental scheme. **(B)** Fast-

1109 tracking imaging regime uses short exposures (10 ms) at high laser power to distinguish
1110 slow (chromatin-bound) and fast (chromatin-free) diffusing populations. **(C)** Slow-tracking
1111 regime directly observes the dwell times of chromatin-bound molecules using 250 ms
1112 exposures at low laser power. (**D-G)** Fast-tracking diffusion histograms for Sth1-Halo (**D**),
1113 Snf2-Halo (**E**), Ino80-Halo (**F**), and Isw2-Halo (**G**). Left: normalized histograms of $\log_{10}$
1114 diffusion coefficients of single-molecule trajectories fitted to two Gaussian distribution
1115 functions (solid gray line: sum of two Gaussians; dashed lines: individual Gaussian curves
1116 representing chromatin-bound and chromatin-free populations). Histograms combined
1117 from 2 or 3 biological replicates are resampled 100 times by the bootstrap method for
1118 resampling errors. Right: Spot-On kinetic modeling results based on displacement
1119 distribution histograms. Solid colored bar with indicated value represents % chromatin-
1120 bound molecules; open bar represents % chromatin-free. Error bars are standard
1121 deviations from 2 or 3 biological replicates.
1122 **Figure supplement 1.** Cell growth, integrity, and localization of HaloTagged remodeler
1123 subunits.
1124 **Figure supplement 2.** Spot-On kinetic modeling analyses.
1125 **Source data 1.** MSD-based kinetic analysis results.
1126
1127 **Figure 2.** Chromatin-binding and chromatin-free populations of CHD1 and ISW1. **(A-B)**
1128 Diffusion coefficient histograms and Spot-On analysis as described in Figure 1 for the
1129 catalytic subunits Chd1-Halo (**A**) and Isw1-Halo (**B**). **(C-D)** Diffusion coefficient
1130 histograms and Spot-On analysis of the accessory subunits of ISW1a and ISW1b
1131 complexes: Ioc3-Halo (**C**) and Ioc4-Halo (**D**).
1132
1133 **Figure 3.** Remodelers undergo frequent transitions between bound and free states. **(A)**
1134 Halo-H2B (brown) and Halo-NLS (pink) molecules display well-separated peaks in their
1135 diffusion coefficient histograms. **(B)** An overview of displacement-based HMM
1136 classification (vbSPT) to identify transitioning trajectories. After classifying each
1137 displacement as either in bound or free state, each trajectory is sub-classified as 'bound
1138 only', 'free only', or 'transitioning'. (**C-I)** Left: Overlay of raw histograms of $\log_{10}$ diffusion
1139 coefficients for 'Bound only' (turquoise), 'Free only' (yellow), 'Transitioning' (purple), and

1140 total trajectories (thin black). Right: Quantification (%) of transitioning trajectories in the
1141 diffusion coefficient histogram, where errors represent standard deviation between 2 or 3
1142 biological replicates. **(C)** Transitioning trajectories for Halo-H2B (top) and Halo-NLS
1143 (bottom). (**D-I)** Transitioning trajectories for remodelers: Sth1-Halo (**D**), Snf2-Halo (**E**),
1144 Ino80-Halo (**F**), and Isw2-Halo (**G**), Chd1-Halo (**H**), and Isw1-Halo (**I**).
1145 **Figure supplement 1.** Validation of two diffusive states classified by vbSPT, and
1146 quantification of transitioning frequencies.
1147 **Source data 1.** vbSPT analysis results.
1148
1149 **Figure 4.** All remodelers have short-lived stable-binding residence times of 4-7 s. **(A-F)**
1150 Fitted double exponential decay curves from 1-CDF plots of observed dwell times from
1151 individual binding events (n) imaged by slow-tracking, for Sth1-Halo (**A**) Snf2-Halo (**B**),
1152 Ino80-Halo (**C**), and Isw2-Halo (**D**), Chd1-Halo (**E**), and Isw1-Halo (**F**). Solid colored and
1153 dashed black fitted curves for indicated remodelers and H2B, respectively. Pie charts
1154 show the percentage (f_{sb}) and average residence time (τ_{sb}) of the stable binding
1155 population after photobleaching correction. Errors represent bootstrap resampling errors
1156 after resampling 100 times (sb: stable-binding; tb: transient-binding).
1157 **Figure supplement 1.** Survival plots [1-CDF] of dwell times showing 1- vs 2-component
1158 exponential decay fits.
1159 **Source data 1.** Kinetic parameters determined by Slow-tracking.
1160
1161 **Figure 5.** ATP hydrolysis is responsible for rapid chromatin dissociation. **(A)** Bar diagram
1162 and cartoons for remodelers mutated in the 'Walker A' and 'Walker B' motifs, respectively.
1163 **(B)** Representative 3D plots of trajectories imaged by slow-tracking for wildtype (Chd1-
1164 Halo, black) and ATPase-dead mutant (Chd1K407R-Halo, red). Each plot shows all
1165 trajectories (≥ 3 frames) from single nucleus where lines represent apparent durations of
1166 chromatin-binding events. **(C-F)** 1-CDF plot, pie chart, and residence times of wildtype
1167 (top) and ATPase-dead mutants (bottom) for Isw2 (**C**), Isw1 (**D**), and Chd1 (**E**,**F**).
1168 **Figure supplement 1.** Expression levels and 1-CDF plots for wildtype and mutant
1169 ATPase-dead Isw2D312N.
1170 **Source data 1.** Slow-tracking results for ATPase-dead mutants.

1171
1172 **Figure 6. ATP utilization is responsible for enhanced mobility of chromatin-bound**
1173 **remodeler. (A-B)** Average MSD plot (**A**) and violin plot (**B**), of individual D values for
1174 'bound only' trajectories imaged by fast-tracking, shown for six remodelers and H2B
1175 histone. **(C)** Violin plot showing distribution of individual D values imaged by slow-tracking
1176 for six remodelers and H2B histone. For (**A-C)** each wildtype remodeler is compared to
1177 H2B by the ordinary one-way ANOVA test (****p<0.0001, ***p<0.001, **p<0.01, *p<0.05).
1178 **(D-H)** MSD plot (**D-F**) and violin plot (**G,H**) of individual D values for 'trajectories imaged
1179 by slow-tracking for wildtype, ATPase-dead mutant, and H2B. For violin plots, thick red
1180 and dotted gray lines represent the median and two quartiles, respectively. For **D-H**,
1181 mutants are compared to wildtype by the unpaired t test (****p<0.0001, ***p<0.001, ns:
1182 not significant). **(I)** Representative trajectories imaged by slow-tracking for H2B and
1183 remodelers. H2B displays low mobility, whereas remodelers display higher chromatin-
1184 associated diffusivity that is enhanced by ATP utilization.
1185 **Figure supplement 1.** Chromatin-bound remodelers display higher radius of
1186 confinement (Rc) values than H2B.
1187 **Source data 1.** Number of molecules (N), statistical tests, and source data for Figure 6.
1188
1189 **Figure 7. Remodelers show substantial temporal occupancies at chromatin targets.**
1190 **(A)** Key parameters measured in this study and acquired from the literature(Ho et al.,
1191 2018; Kubik et al., 2019) are used to calculate occupancy levels for gene promoter-acting
1192 remodelers. **(B)** Time trace simulations of temporal occupancy for individual remodelers
1193 at a target promoter region based on average τ_{sb} and sampling interval. Top and bottom
1194 bars represent occupied (on) and vacant (off) states, respectively, and vertical lines depict
1195 transitions between the two states. **(C)** Time trace simulations of occupancy at a RSC-
1196 and INO80-bound promoter region based on average τ_{sb} and sampling interval. Individual
1197 time trace simulations are shown above, and the cumulative simulated occupancy plot
1198 (black) shows either one or both remodelers bound in the time course of 500 s.
1199 **Figure supplement 1.** Time trace simulations of temporal occupancies at promoters
1200 bound by multiple remodelers, and analysis of CHD1 DNA-binding mutant.
1201

1202 **Figure 8. Nucleosome remodeling cycle at NDRs.** Model for nucleosome remodeling
1203 cycle at a gene promoter region targeted by RSC and INO80. The promoter region
1204 transitions between remodeler-occupied [solid arrow] and -vacant [dashed arrow] states,
1205 and their durations are indicated. After association of RSC or INO80 to the NDR,
1206 remodelers undergo 1-D diffusion on chromatin in an ATP-dependent manner, resulting
1207 in higher chromatin-associated mobility. Upon engaging its nucleosome substrate [e.g.
1208 the +1 nucleosome], RSC and INO80 uses the energy of ATP hydrolysis to push or pull
1209 the nucleosome away from NDR, respectively. ATP hydrolysis facilitates remodeler
1210 dissociation, and the promoter region becomes vacant for other factor interactions. The
1211 order of remodeler visitation is arbitrary, and simultaneous co-occupancy within the NDR
1212 can occur infrequently (see text for details).
1213
1214 **SUPPLEMENTAL INFORMATION**
1215 **Figure 1-figure supplement 1. Cell growth, integrity, and localization of HaloTagged**
1216 **remodeler subunits.**
1217 **(A)** SDS-PAGE gel scanned for JF646 dye fluorescence (top) and imaged after
1218 Coomassie staining (bottom). Cell lysates are prepared after treatment with JF646 at a
1219 saturating dye concentration (20 nM) for 2 h at 30°C. **(B)** Overlay of Phase Contrast image
1220 and 'nuclear glow' captured by initial JF552 dye excitation of yeast stained with JF552.
1221 **(C)** Five-fold dilutions of HaloTag fusion and wildtype strains are plated on YPAD plates
1222 at the indicated temperatures for 2-3 days. **(D)** Relationship between D_{free} values
1223 determined by Spot-On analysis and the calculated molecular weights of chromatin
1224 remodeling complexes.
1225
1226 **Figure 1-figure supplement 2. Spot-On kinetic modeling analyses.**
1227 **(A)** Kinetic parameters (F_{bound}, D_{bound}, D_{free}) determined by Spot-On analyses. Errors
1228 represent standard deviation between 2 or 3 biological replicates. **(B)** Raw displacement
1229 histograms for individual biological replicates over the first 5 time frames (Δt: 10, 20, 30,
1230 40, 50 ms). A two-state kinetic model was used for fitting the CDF [black lines] in Spot-
1231 On. F_{bound} values (shown above the histograms) are highly reproducible between
1232 replicates.

1233

1234 **Figure 3-figure supplement 1. Validation of two diffusive states classified by vbSPT,**
1235 **and quantification of transitioning frequencies.**
1236 **(A)** Pipeline for classification and sub-classification of trajectories using vbSPT. Individual
1237 displacement lengths were determined for 'bound only', 'free only', and 'transitioning'-
1238 subclassified trajectories to validate the two states and state transitions. **(B-C)** Violin plot
1239 (**B**) and median value (**C**) of individual displacement lengths for the Bound and Free states
1240 in non-transitioning and transitioning trajectories. For violin plots, thick red and dotted
1241 gray lines represent the median and two quartiles, respectively. **(D-E)** Transitioning
1242 trajectories for Ioc3-Halo (**D**) and Ioc4-Halo (**E**). Left: Overlay of raw histograms of $\log_{10}$
1243 diffusion coefficients for 'Bound only' (turquoise), 'Free only' (yellow), 'Transitioning'
1244 (purple), and total trajectories (thin black). Right: Quantification (%) of transitioning
1245 trajectories in the diffusion coefficient histogram. **(F)** For all classified transitioning
1246 trajectories, 'FREE' to 'BOUND' and 'BOUND' to 'FREE' transition frequencies are
1247 indicated. For **D-F,** errors represent standard deviation between 2 or 3 biological
1248 replicates.
1249

1250 **Figure 4-figure supplement 1. Survival plots [1-CDF] of dwell times showing 1- vs**
1251 **2-component exponential decay fits.**
1252 **(A-F)**1- and 2-component exponential decay fits to survival plots of dwell times for Sth1-
1253 Halo (**A**), Snf2-Halo (**B**), Ino80-Halo (**C**), and Isw2-Halo (**D**), Chd1-Halo (**E**), and Isw1-
1254 Halo (**F**). **(G)** 1-CDF plot, pie chart as in Figure 4, and residence times of Ioc3-Halo (Left)
1255 and Ioc4-Halo (Right). **(H)** 1- and 2-component exponential decay fits to survival plots of
1256 dwell times for Ioc3-Halo (Left) and Ioc4-Halo (Right).
1257

1258 **Figure 5-figure supplement 1. Expression levels and 1-CDF plots for wildtype and**
1259 **mutant ATPase-dead Isw2D312N.**
1260 **(A)** SDS-PAGE analysis; gel scanned for JF646 dye fluorescence (top) and imaged after
1261 Coomassie staining (bottom). Cell lysates of ATPase mutants (Isw1K227R-Halo,
1262 Isw2K215R-Halo and Chd1D513N-Halo) and their wildtype strains were prepared after
1263 treatment with JF646 at a saturating dye concentration (20 nM) for 2 h at 30oC. **(B-E)**1-

1264 CDF plot in log-log scale for Isw2K215R (**B**), Isw1K227R (**C**), Chd1K407R (**D**), and
1265 Chd1D513N (**E**) compared to wildtype. Colored dashed lines represent 95% confidence
1266 interval.
1267
1268 **Figure 6-figure supplement 1. Chromatin-bound remodelers display higher radius**
1269 **of confinement (Rc) values than H2B.**
1270 **(A)** Radius of confinement values of bound trajectories in 10-ms exposure movies for
1271 histone H2B and chromatin remodelers. Violin plot showing distribution of R_c values, and
1272 comparison between histone H2B and each of wildtype remodelers by ordinary one-way
1273 ANOVA test. **(B)** Violin plot of individual D values by slow-tracking for Isw1-Halo after 30
1274 min pre-treatment with 3 or 5 ug/mL thiolutin, and comparison between wildtype and
1275 thiolutin-treated samples by unpaired t test (ns: not significant). Thick red and dotted gray
1276 lines represent the median and two quartiles, respectively.
1277
1278 **Figure 7-figure supplement 1. Time trace simulations of temporal occupancies at**
1279 **promoters bound by multiple remodelers, and analysis of CHD1 DNA-binding**
1280 **mutant.**
1281 **(A-B)** Time trace simulations of occupancy as in Figure 6, at a promoter region bound by
1282 RSC, INO80, and ISW2 remodelers (**A**) or by RSC, SWI/SNF, INO80, and ISW2
1283 remodelers (**B**). Individual time trace simulations are shown above, and the cumulative
1284 simulated occupancy time trace (black) shows any one or multiple remodelers bound in
1285 the time course of 500 s. **(C-D)** Fast-tracking and slow-tracking results for CHD1 DNA-
1286 binding domain mutant (Chd1R1016A/K1020A/R1255A-Halo). (wildtype: dashed gray
1287 lines; DBD mutant: solid green lines). (**C**) Normalized histogram $\log_{10}$ diffusion coefficients
1288 (Left) and Spot-On kinetic modeling results (Right). (**D**) 1-CDF plot, pie chart, and
1289 residence times.
1290
1291 **Supplementary file 1. List of Yeast strains used in the study**
1292 **Supplementary file 2. List of oligonucleotides used in the study**

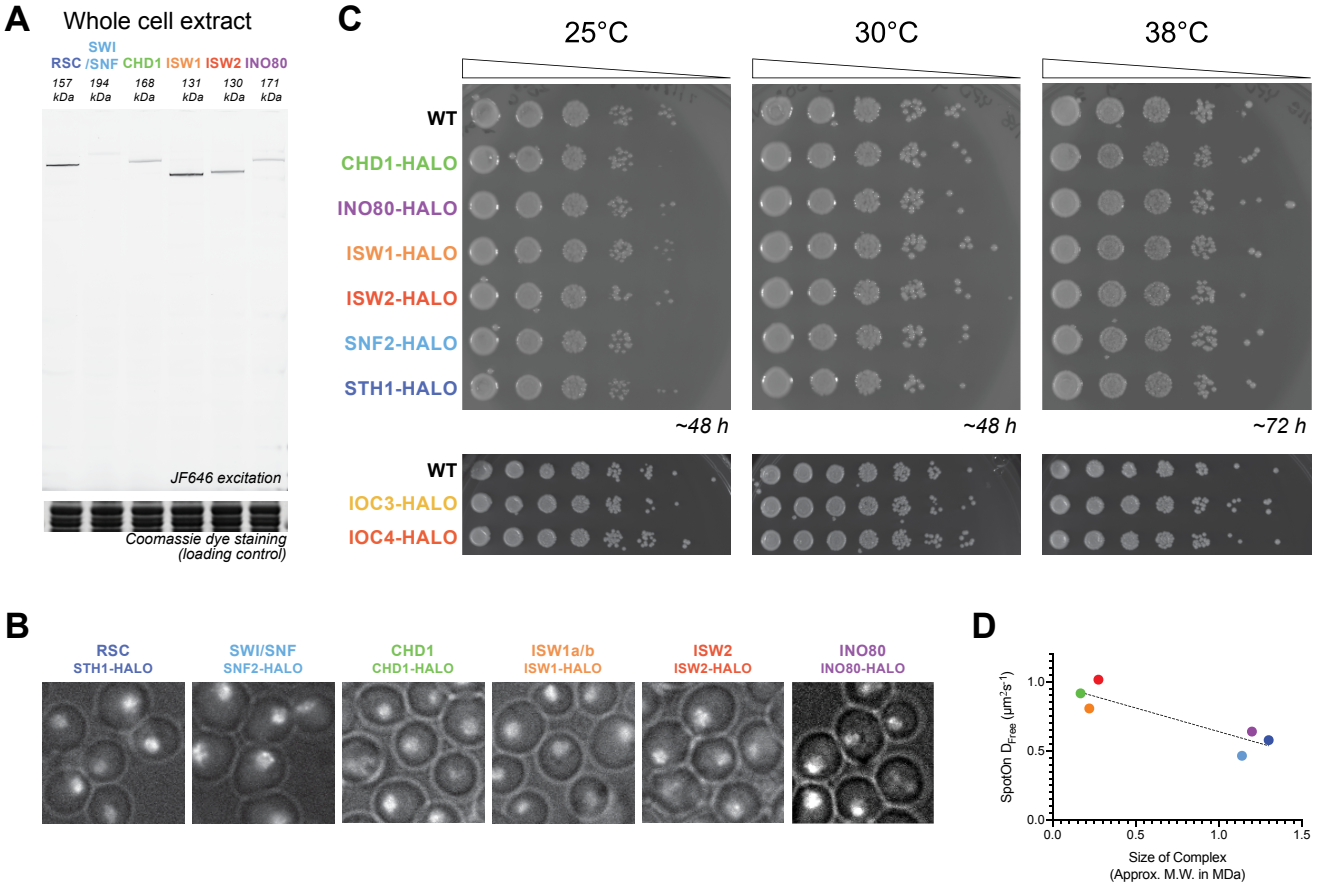

Figure 1-figure supplement 1. Cell growth, integrity, and localization of HaloTagged remodeler subunits.

(A) SDS-PAGE gel scanned for JF646 dye fluorescence (top) and imaged after Coomassie staining (bottom). Cell lysates are prepared after treatment with JF646 at a saturating dye concentration (20 nM) for 2 h at 30°C. **(B)** Overlay of Phase Contrast image and 'nuclear glow' captured by initial JF552 dye excitation of yeast stained with JF552. **(C)** Five-fold dilutions of HaloTag fusion and wildtype strains are plated on YPAD plates at the indicated temperatures for 2-3 days. **(D)** Relationship between D_{free} values determined by Spot-On analysis and the calculated molecular weights of chromatin remodeling complexes.

A

Remodeler	F_{bound} (%)	D_{bound} ($\mu m^2 s^{-1}$)	D_{free} ($\mu m^2 s^{-1}$)
RSC (Sth1)	66.0 ± 1.1	0.038 ± 0.002	0.577 ± 0.069
SWI/SNF (Snf2)	55.9 ± 1.3	0.036 ± 0.007	0.464 ± 0.043
INO80 (Ino80)	48.3 ± 0.2	0.050 ± 0.004	0.639 ± 0.058
ISW2 (Isw2)	35.4 ± 0.4	0.062 ± 0.001	1.014 ± 0.024
CHD1 (Chd1)	47.8 ± 4.9	0.047 ± 0.007	0.915 ± 0.038
ISW1a/b (Isw1)	52.0 ± 1.1	0.050 ± 0.001	0.806 ± 0.010
ISW1a (Ioc3)	39.6 ± 0.0	0.067 ± 0.004	0.791 ± 0.059
ISW1b (Ioc4)	55.5 ± 2.6	0.044 ± 0.005	0.532 ± 0.042
Histone H2B	79.4 ± 1.9	0.026 ± 0.000	0.970 ± 0.158

B

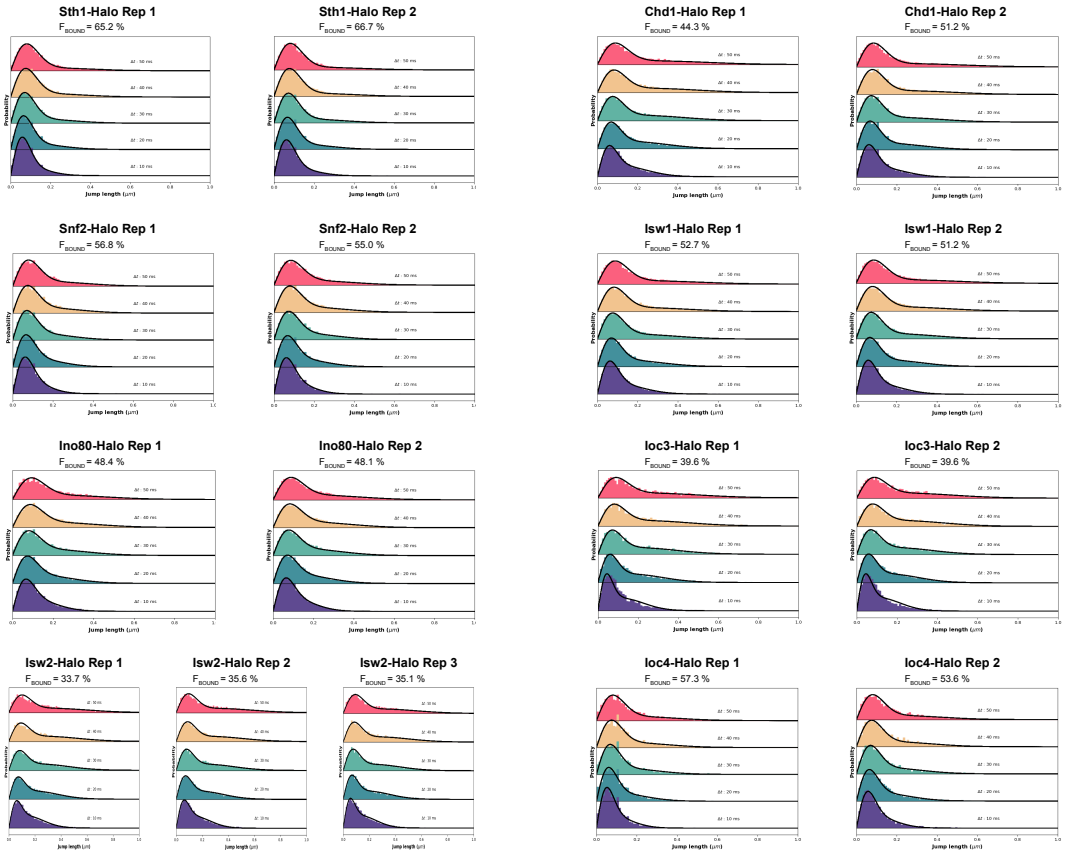

Figure 1-figure supplement 2. Spot-On kinetic modeling analyses.
(A) Kinetic parameters (F_{bound}, D_{bound}, D_{free}) determined by Spot-On analyses. Errors represent standard deviation between 2 or 3 biological replicates. **(B)** Raw displacement histograms for individual biological replicates over the first 5 time frames (Δt: 10, 20, 30, 40, 50 ms). A two-state kinetic model was used for fitting the CDF [black lines] in Spot-On. F_{bound} values (shown above the histograms) are highly reproducible between replicates.

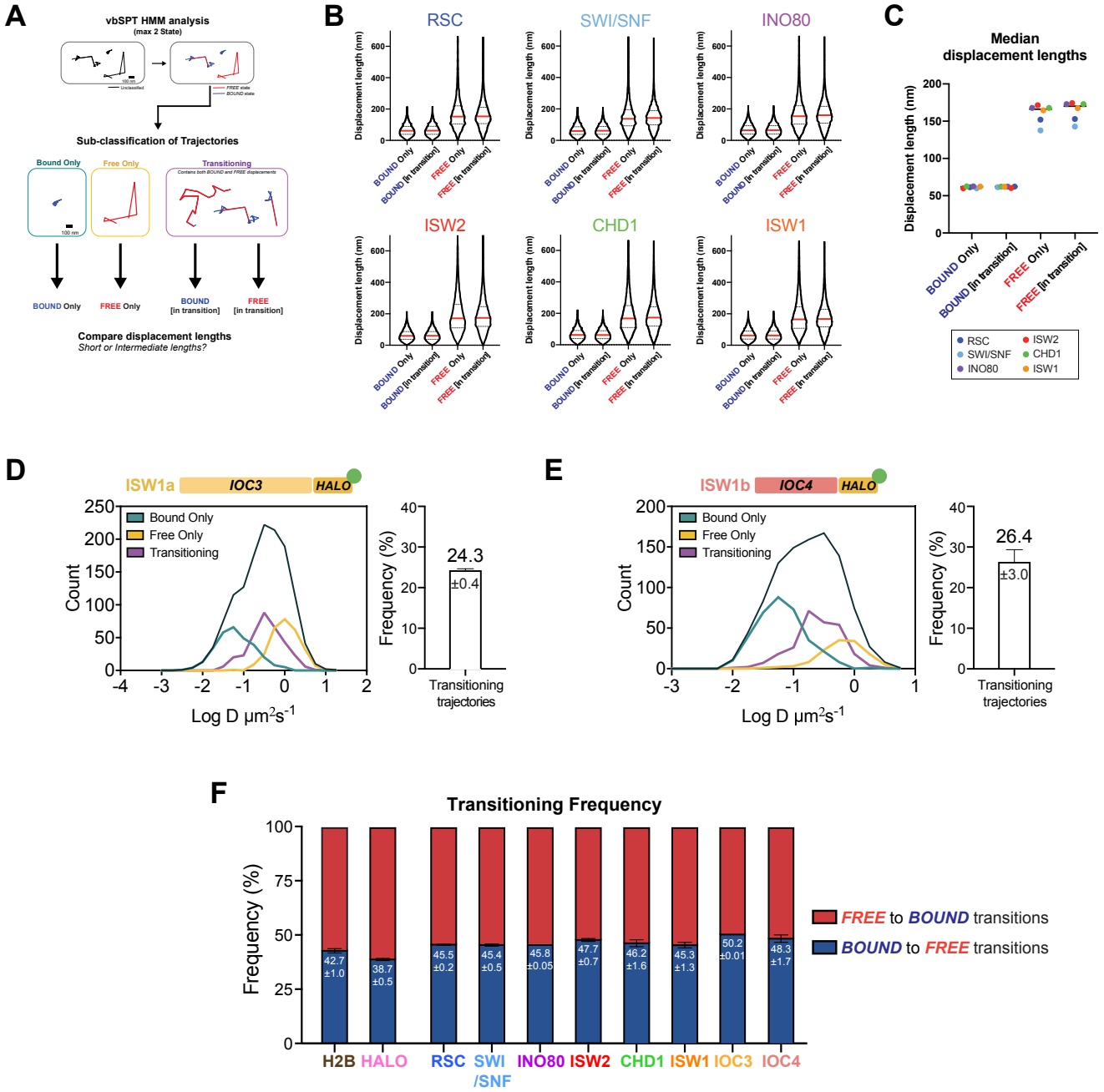

Figure 3-figure supplement 1. Validation of two diffusive states classified by vbSPT, and quantification of transitioning frequencies.

(A) Pipeline for classification and sub-classification of trajectories using vbSPT. Individual displacement lengths were determined for 'bound only', 'free only', and 'transitioning'-subclassified trajectories to validate the two states and state transitions. **(B-C)** Violin plot (**B**) and median value (**C**) of individual displacement lengths for the Bound and Free states in non-transitioning and transitioning trajectories. For violin plots, thick red and dotted gray lines represent the median and two quartiles, respectively. **(D-E)** Transitioning trajectories for Ioc3-Halo (**D**) and Ioc4-Halo (**E**). Left: Overlay of raw histograms of $\log_{10}$ diffusion coefficients for 'Bound only' (turquoise), 'Free only' (yellow), 'Transitioning' (purple), and total trajectories (thin black). Right: Quantification (%) of transitioning trajectories in the diffusion coefficient histogram. **(F)** For all classified transitioning trajectories, 'FREE' to 'BOUND' and 'BOUND' to 'FREE' transition frequencies are indicated. For **D-F**, errors represent standard deviation between 2 or 3 biological replicates.

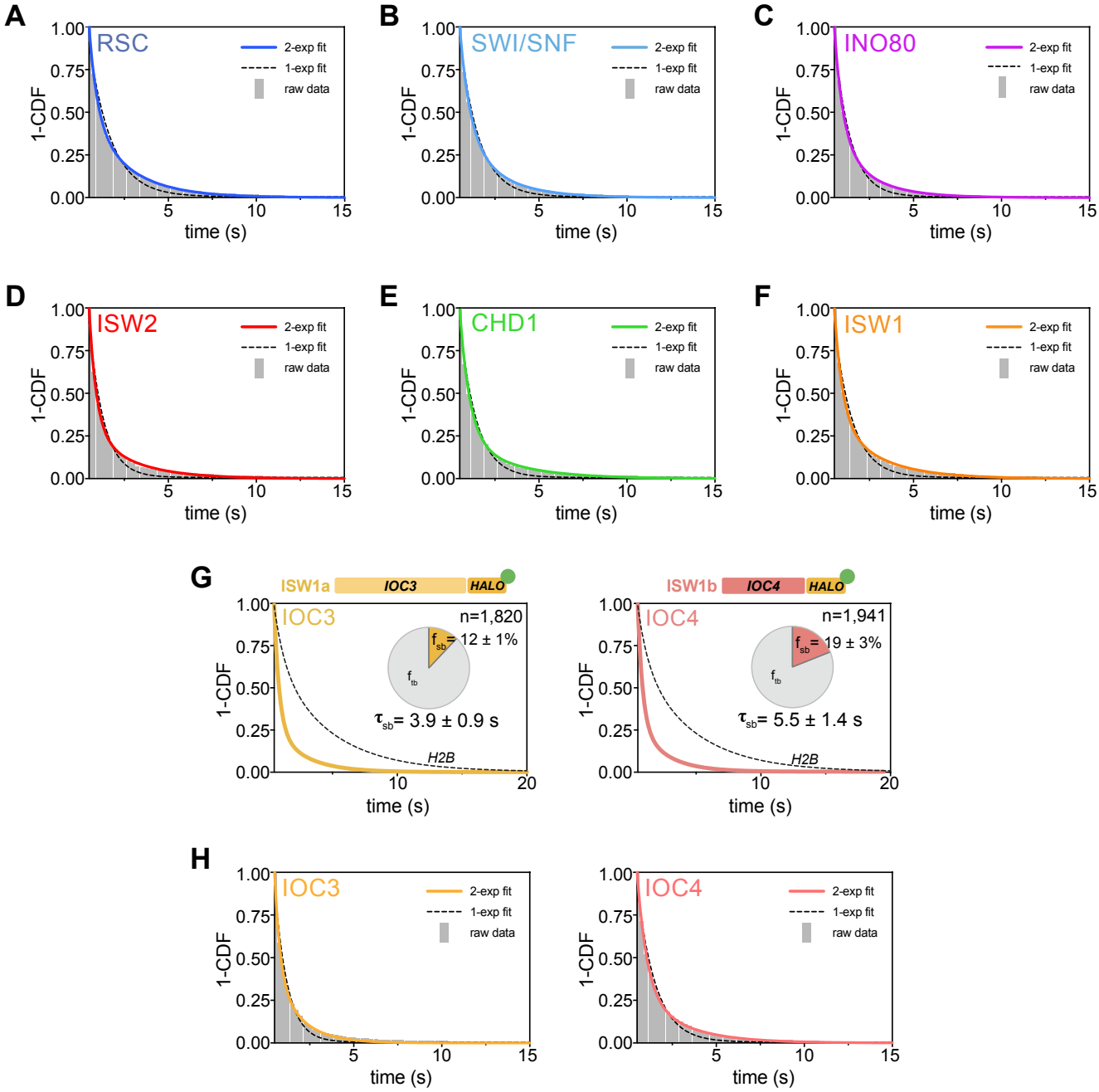

Figure 4-figure supplement 1. Survival plots [1-CDF] of dwell times showing 1- vs 2-component exponential decay fits.

(A-F)1- and 2-component exponential decay fits to survival plots of dwell times for Sth1-Halo (**A**), Snf2-Halo (**B**), Ino80-Halo (**C**), and Isw2-Halo (**D**), Chd1-Halo (**E**), and Isw1-Halo (**F**). **(G)** 1-CDF plot, pie chart as in Fig. 4, and residence times of Ioc3-Halo (Left) and Ioc4-Halo (Right). **(H)** 1- and 2-component exponential decay fits to survival plots of dwell times for Ioc3-Halo (Left) and Ioc4-Halo (Right).

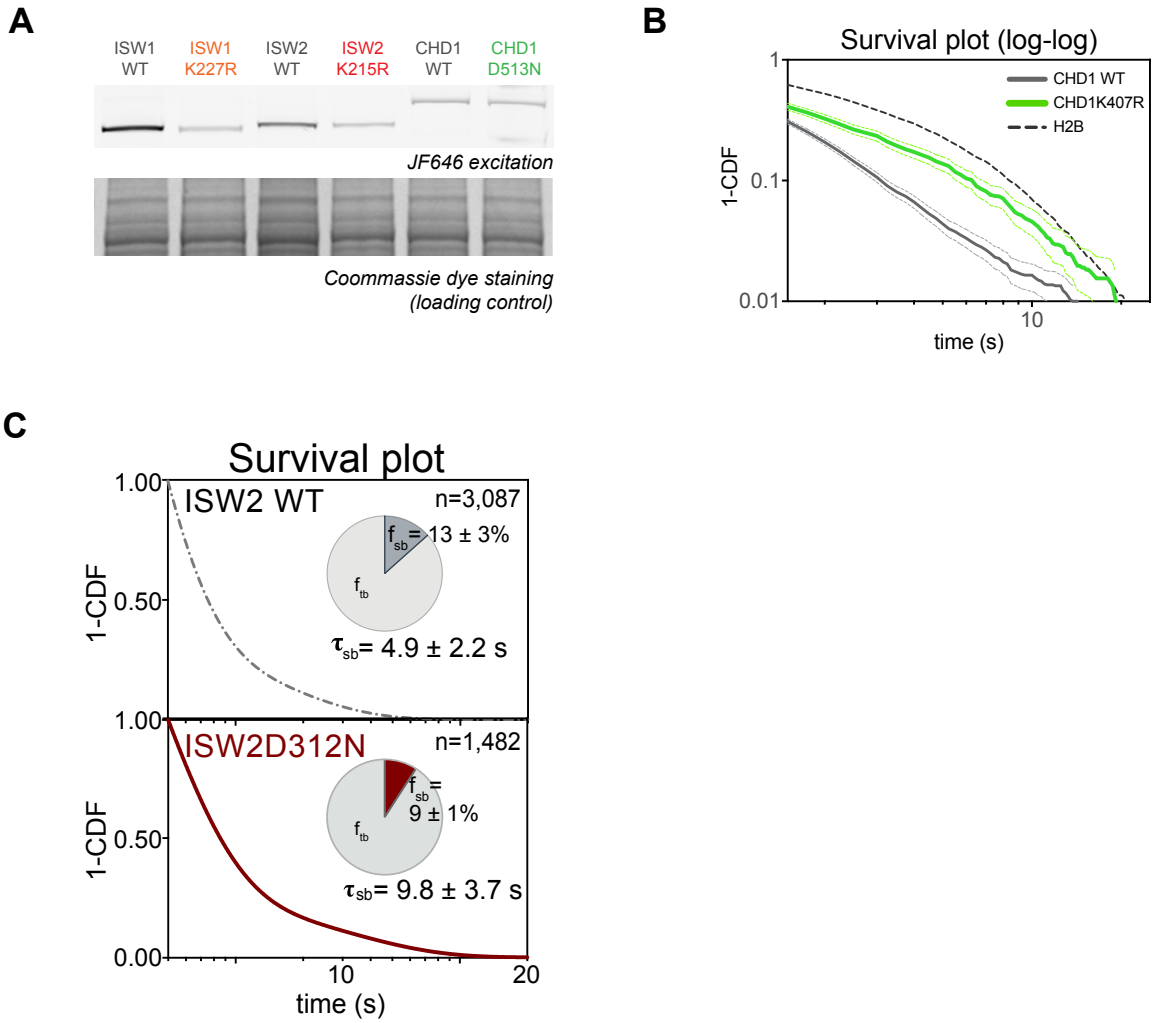

Figure 5-figure supplement 1. Expression levels and 1-CDF plots for wildtype and mutant ATPase-dead Isw2D312N.

(A) SDS-PAGE analysis; gel scanned for JF646 dye fluorescence (top) and imaged after Coomassie staining (bottom). Cell lysates of ATPase mutants (Isw1K227R-Halo, Isw2K215R-Halo and Chd1D513N-Halo) and their wildtype strains were prepared after treatment with JF646 at a saturating dye concentration (20 nM) for 2 h at 30°C. **(B)** 1-CDF plot in log-log scale for Chd1K407R compared to wildtype. Colored dashed lines represent 95% confidence interval. **(C)** 1-CDF plot, pie chart, and residence times of wildtype Isw2-Halo (top) and Isw2D312N-Halo (bottom).

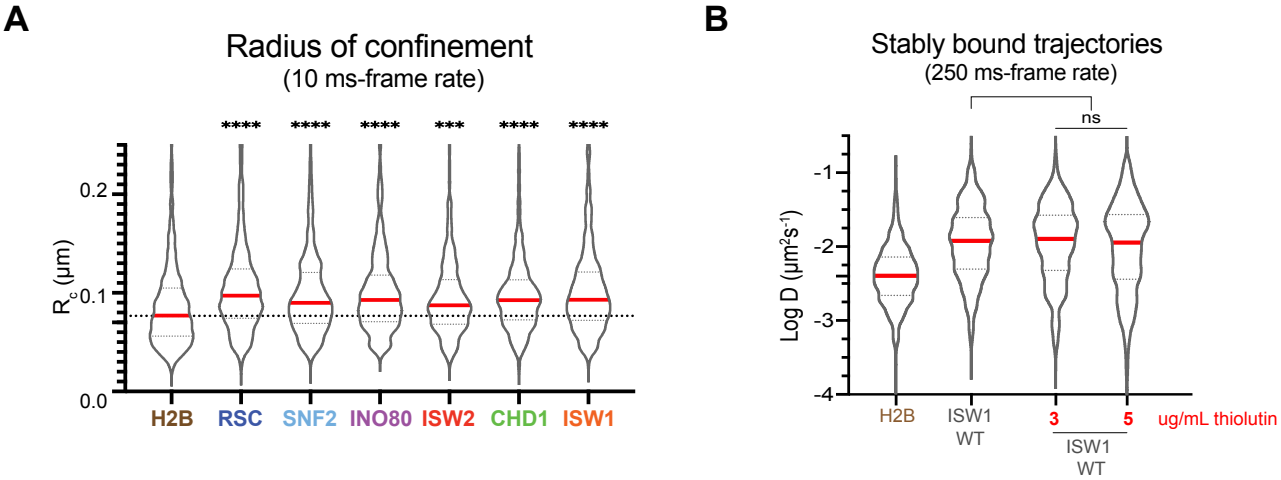

Figure 6-figure supplement 1. Chromatin-bound remodelers display higher radius of confinement (R_c) values than H2B.
(A) Radius of confinement values of bound trajectories in 10-ms exposure movies for histone H2B and chromatin remodelers. Violin plot showing distribution of R_c values, and comparison between histone H2B and each of wildtype remodelers by ordinary one-way ANOVA test. **(B)** Violin plot of individual D values by slow-tracking for Isw1-Halo after 30 min pre-treatment with 3 or 5 ug/mL thiolutin, and comparison between wildtype and thiolutin-treated samples by unpaired t test (ns: not significant). Thick red and dotted gray lines represent the median and two quartiles, respectively.

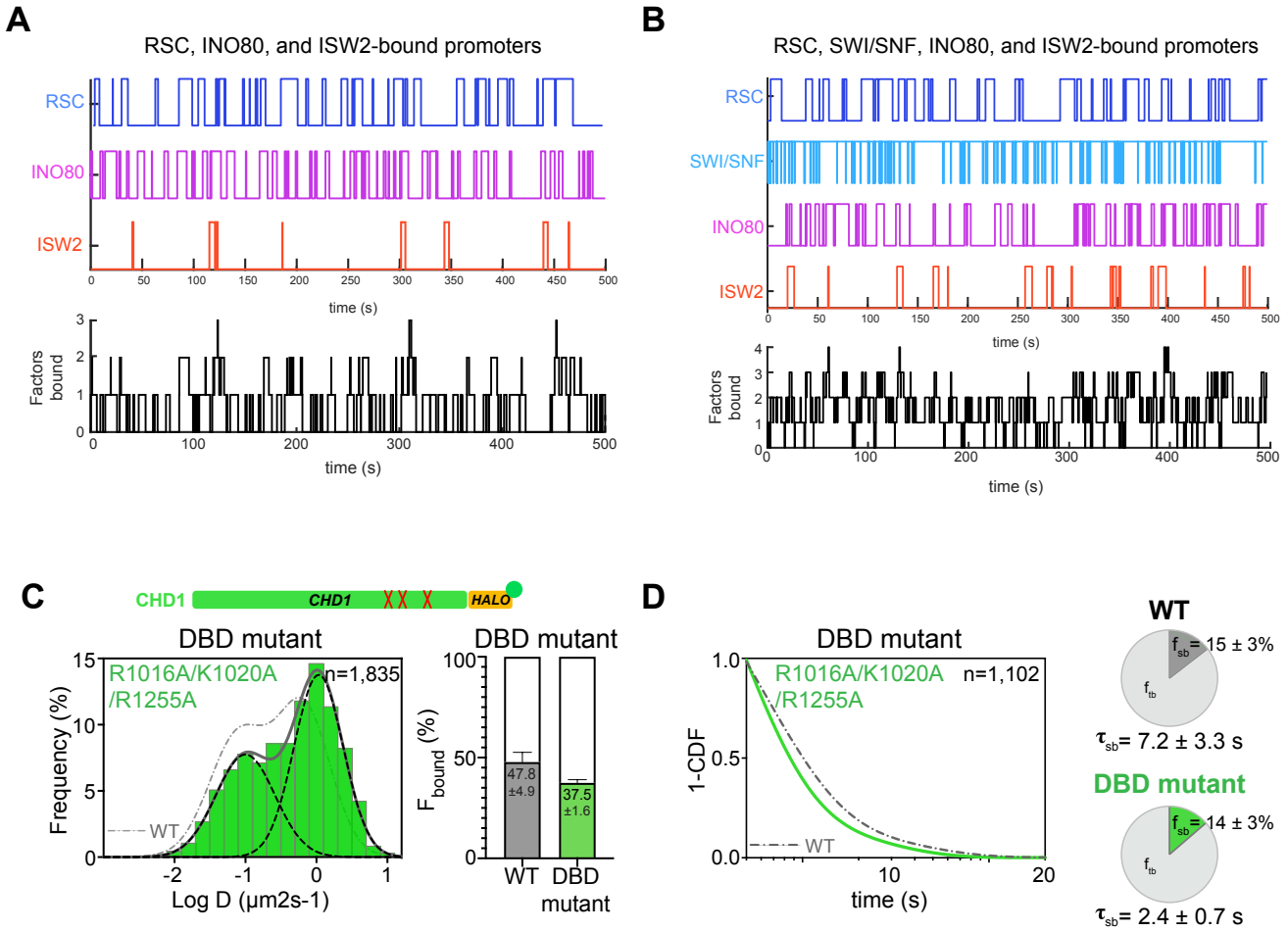

Figure 7-figure supplement 1. Time trace simulations of temporal occupancies at promoters bound by multiple remodelers, and analysis of CHD1 DNA-binding mutant.

(A-B) Time trace simulations of occupancy as in Fig. 6, at a promoter region bound by RSC, INO80, and ISW2 remodelers (**A**) or by RSC, SWI/SNF, INO80, and ISW2 remodelers B). Individual time trace simulations are shown above, and the cumulative simulated occupancy time trace (black) shows any one or multiple remodelers bound in the time course of 500 s. **(C-D)** Fast-tracking and slow-tracking results for CHD1 DNA-binding domain mutant (Chd1R1016A/K1020A/R1255A-Halo). (wildtype: dashed gray lines; DBD mutant: solid green lines). (**C**) Normalized histogram $\log_{10}$ diffusion coefficients (Left) and Spot-On kinetic modeling results (Right). (**D**) 1-CDF plot, pie chart, and residence times.